UNIVERSITY OF CALIFORNIA,
IRVINE

Predicting Individual Cardiomyocyte Myofibril Organization In Spatially Constrained Cells

DISSERTATION

submitted in partial satisfaction of the requirements
for the degree of

DOCTOR OF PHILOSOPHY

in Mathematical, Computational, and Systems Biology

by

William Sherman

Dissertation Committee:
Associate Professor Anna Grosberg, Chair
Assistant Professor Elizabeth Read
Professor Charless Fowlkes

2020

DEDICATION

This dissertation is dedicated to my family, friends, and mentors that have guided me through this journey. To my mom and dad, who always supported me in pursuing higher education. To my brother and sister-in-law for all of their enthusiasm and encouragement over the seemingly endless years of research and study. And to the many mentors I have had throughout my academic career, especially Dr. Ramin Vakilian, who guided me through my formative years in the Mathematics Department at CSU Northridge. Lastly, to Anneka for being my rock and helping me see the light at the end of the tunnel. I don't know how I would have completed the last stretch of my research without her by my side and her unwavering support. Each person undoubtably inspired me on my journey and has, in one way or another, given me the confidence to pursue and complete a doctorate.

TABLE OF CONTENTS

LIST OF FIGURES

ACKNOWLEDGMENTS

I would like to thank my family and friends for their support over these many years.

This work was partially supported by the Edwards Lifesciences Center for Advanced Cardiovascular Technology's NIH/NHLBI T32HL116270 Training Grant, National Science Foundation DMS1763272 and a grant from the Simons Foundation 594598.

Also, I would like to thank Mira Asad for her help in gathering the experimental data used in this work.

Lastly, I would like to acknowledge the publishers of Wiley Interdisciplinary Reviews: Systems Biology and Medicine, AIP Advances, and PLOS Computational Biology for allowing me to incorporate my previous work in my dissertation. Chapter 1 was published with the permission of John Wiley & Sons, Inc. The text and figures of this chapter is a reprint of the material as it appears in Wiley Interdisciplinary Reviews: Systems Biology and Medicine. I also thank AIP Publishing for permission to include Chapter 2 of my dissertation, which was originally published in AIP Advances. The text and figures of Chapter 3 was submitted in its entirety for publication in PLOS Computational Biology and is currently under peer review.

VITA

William Sherman

Education

Ph.D. in Mathematical, Computational and Systems Biology **2020**
University of California, Irvine *Irvine, CA*

M.S. in Mathematics **2014**
California State University, Northridge *Northridge, CA*

B.S. in Classical Applied Mathematics **2012**
California State University, Northridge *Northridge, CA*

Research Experience

Graduate Student Researcher **2014–2020**
University of California, Irvine *Irvine, CA*

Graduate Student Researcher **2012–2014**
California State University, Northridge *Northridge, CA*

Teaching Experience

Graduate Teaching Assistant **2019–2020**
University of California, Irvine *Irvine, CA*

Graduate Teaching Assistant **2012–2014**
California State University, Northridge *Northridge, CA*

Refereed Journal Publications

Exploring cardiac form and function: A length-scale computational biology approach **2020**
WIREs Syst Biol Med

An adapted particle swarm optimization algorithm as a model for exploring premyofibril formation **2020**
AIP Advances

A dynamic energy minimization model for cytoskeletal organization **2020**
Submitted

ABSTRACT OF THE DISSERTATION

Predicting Individual Cardiomyocyte Myofibril Organization In Spatially Constrained Cells

By

William Sherman

Doctor of Philosophy in Mathematical, Computational, and Systems Biology

University of California, Irvine, 2020

Associate Professor Anna Grosberg, Chair

Through a variety of mechanisms, a healthy heart is able to regulate its structure and dynamics across multiple length scales. Disruption of these mechanisms can have a cascading effect, resulting in severe structural and/or functional changes that permeate across different length scales. Due to this hierarchical structure, there is interest in understanding how the components at the various scales coordinate and influence each other. While there has been much progress at the molecular scale, there is a growing need for theoretical models to address interactions at the cellular and subcellular scales. In particular, understanding the mechanisms guiding the formation and organization of the cytoskeleton in individual cardiomyocytes can aid tissue engineers in developing functional cardiac tissue.

In this dissertation, we developed computational models which integrate interactions at both the cellular and subcelluar scale to enhance our understanding of how cardiomyocytes self-assemble at different length scales. Experimental data, which consisted of single cell cardiomyocytes having fixed area but variable aspect ratio, was used to test and validate our models. Cells were analyzed for structural consistency and contractility using established metrics. The metrics where then applied to our model simulations for comparison. We demonstrated that our model simulations are capable of reproducing the stochasticity observed in experimental cells at different length scales while also mimicking structural con-

sistency. In addition to recreating known patterns present in the experimental cells, our models have provided insight towards possible mechanisms that can be explored by experimentalists.

Chapter 1

Exploring cardiac form and function: A length-scale computational biology approach

[1]

1.1 Introduction

The primary function of the heart is to pump blood in a stable and efficient manner. Native heart tissue consists of aligned interlocking cardiac cells. These individual cardiomyocytes contain myofibrils composed of patterns of repeating sarcomeres, which themselves incorporate a variety of organized interacting proteins [108, 3, 19] (Fig. 1.1). Each of these individual components work in concert to induce a contraction [51, 94], from the laminar sheets that make up the heart's four chambers [99] to the individual proteins within the actin-mysoin

[1] W. F. Sherman and A. Grosberg, 2020 WIREs Syst Biol Med

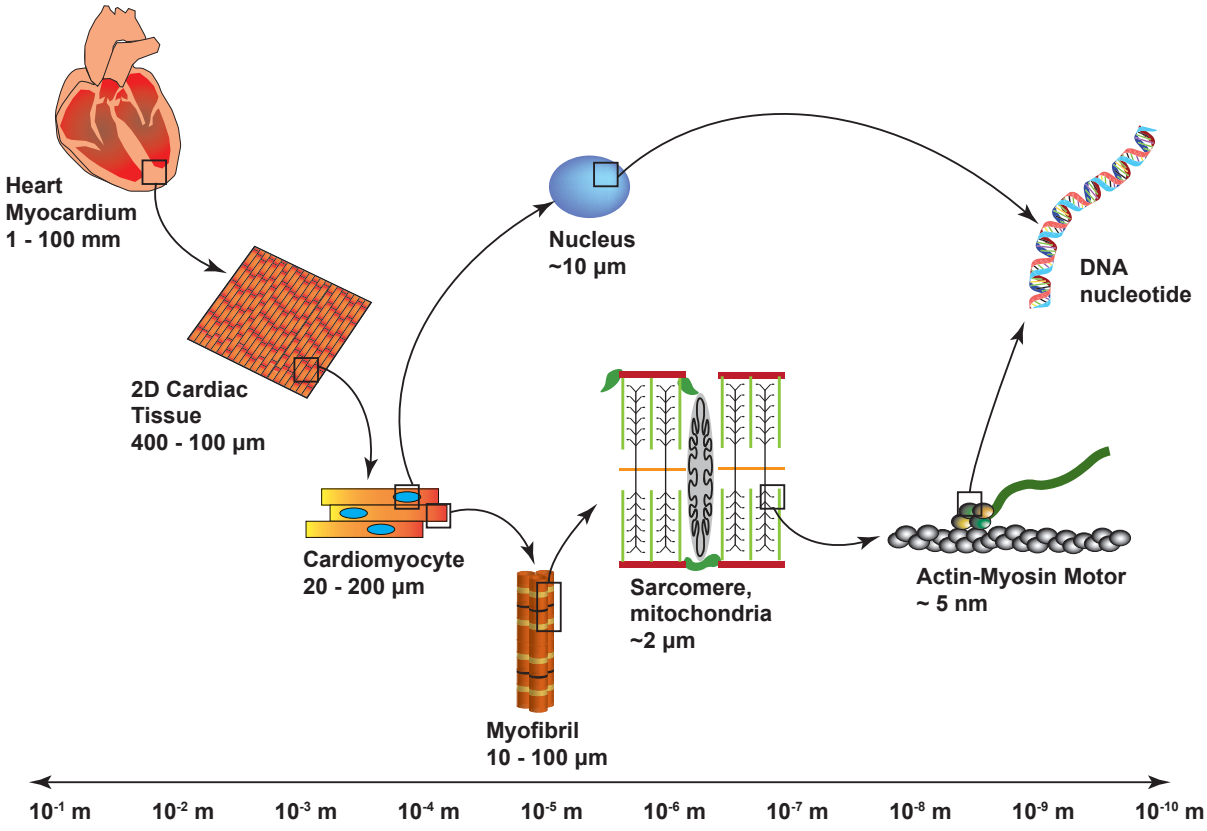

Figure 1.1. Length scale separation within the heart. Spatial scales can be broken down into a hierarchical structure that spans several orders of magnitude. The various functional components can be studied either independently or in relation to one another.

motors [24]. Recapitulating the cooperative nature of this multi-scale coordination is a cornerstone of cardiac tissue engineering [146, 122]. To build tissue that is functional and adaptable requires an understanding of how chemical and biomechanical signals are translated across hierarchical scales as well as the relation between form and function within an individual scale. Through development of *in vitro* models that mimic the appearance and pathology of native healthy tissue, researchers can explore the factors that influence the various structural patterns present *in vivo* such as myofibril alignment and sarcomeric registration [94, 31]. However, while these studies suggest correlations between structural parameters and cell morphology, they do not address how physical cues drive self-organization. An ideal method to study the causal relation between proposed parameters is to use com-

putational modeling. In this way, researchers can target specific variables and explore their roles, providing insight into how the identified components cooperate to guide self-assembly. Numerous computational models have been proposed and they can be broadly classified based on the spatial scale of interest.

Models at the organ and tissue scale typically focus on functionality and explore the influence of cell-cell interactions on tissue-level characteristics such as orientation, beating rate, and contractile strength [23, 36, 57, 12]. In single cells, the ability to self-organize depends on extracellular matrix (ECM) interactions. As such, models at this scale are often concerned with the mechanical cues that influence these interactions [35, 86, 106]. At the sub-cellular scale, however, the proper computational approach depends on the structure of interest [40, 129, 47]. This results in a wide variety of modeling techniques and considerations. To adequately contribute to the field using a modeling approach requires one to not only identify areas which may benefit from computational modeling but also utilize methodologies that are appropriate for the area of interest. Considering the breadth of approaches that have been employed, new researchers with a desire to utilize computational modeling may find the task daunting. We will provide the first step to tackling this problem by identifying common model types that are used at certain spatial scales and summarizing their strengths and weaknesses.

This review will explore the cardiac structure hierarchy through the lens of systems biology, which can be described as an amalgamation of principles from fields such as biology, engineering, and computer science. Beginning at the organ (centimeter to millimeter) scale and continuing to the sub-cellular (nanometer) scale, we will provide an overview of common modeling techniques found in the literature and some of the notable results that those techniques have provided. We then give an overview of the advantages and drawbacks associated with combining models from several scales into a singular multi-scale model. Emphasis will be placed on the interplay between the experimental observations and the modeling ap-

proaches since the feedback between experimental techniques and theoretical testing is core to the systems biology approach.

Since the heart is a highly complex, multi-scaled organ, we have chosen to focus our attention towards specific areas of cardiovascular research related to mechanical function. As such, there are numerous areas of active research that will not be covered in this review and are left to the references. These include ionic channel kinetics and their association with contractile function [141, 112], models focusing on cardiac electrophysiology [79], and application of fluid mechanics to blood flow and circulation [101], to name a few.

1.2 Modeling approaches at the organ and tissue scale

Heart failure, due to some form of cardiovascular disease, is frequently cited as a leading cause of death worldwide [15, 132, 93, 98] and once sever damage has occurred, a heart transplant may be the only form of repair. Due to a limited supply of donor hearts [116, 75], efforts have been made to develop protocols for exploring regenerative and preventative medicines. This has led many to study how alterations to cardiac properties, processing, and structure affect the heart's performance, summarized by the materials science tetrahedron (Fig. 1.2). Specifically, focus is often placed on two separate yet interconnected properties: construct development and functionality. While it is useful to address the interplay between these two fundamental characteristics, organ and tissue scale models tend to emphasize the impact on functionality. An overarching goal of organ level modeling is to create a mathematical representation of the heart with tunable parameters that are patient-specific. The hope is that these whole-heart computational models will allow physicians to explore ventricular remodeling, electrophysiology and blood flow in a non-invasive manner so that customizable therapies can be developed. To adequately cover the progress that has been made at this level, we feel an entire review is warranted. As such, we refer the reader to the work being

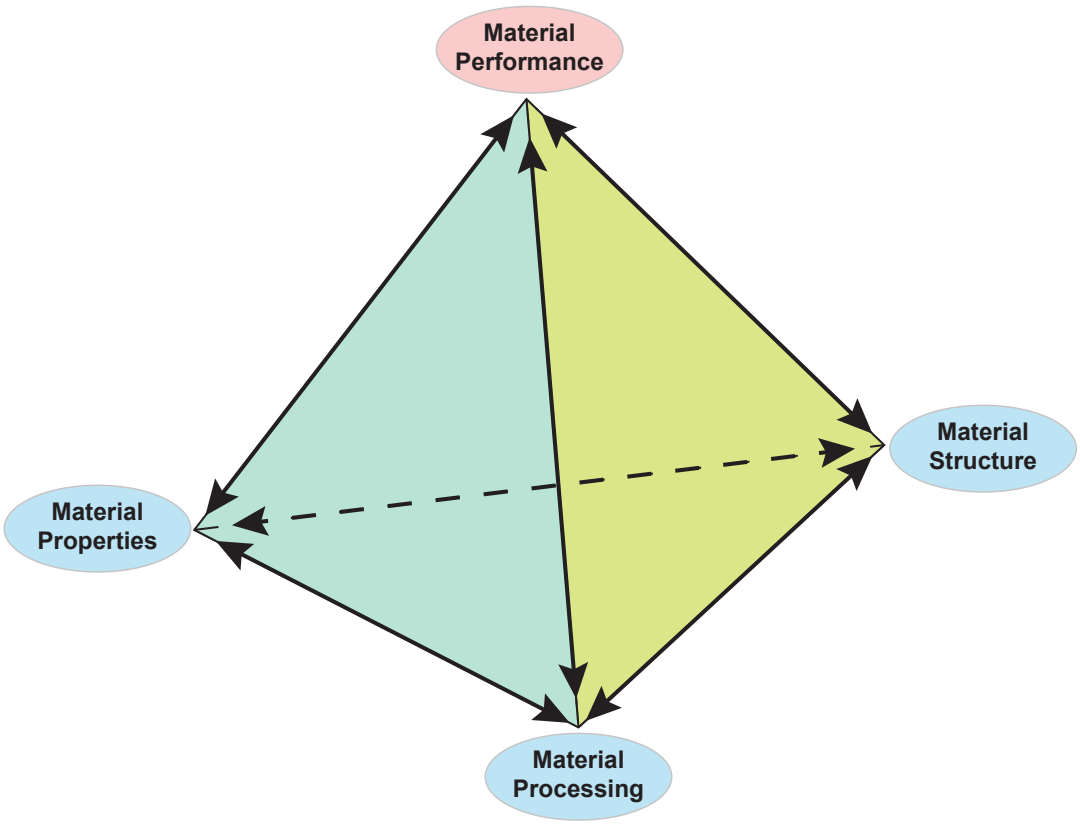

Figure 1.2. The materials science tetrahedron. There are four interconnected categories that can be used to study the behavior of a material: structure, processing, properties, and performance. Changes in any one category will invariable influence the other three categories. This same categorization may be used to study the heart. (Adapted from [51])

done by McCulloch and colleagues [27, 130], Trayanova and associates [143, 124], as well as Peskin and McQueen [60], among many others, for advancements at this scale.

Engineering a functional tissue *in vitro* entails guiding cell assembly through targeted changes in the cellular environment. These changes can be achieved, for example, by using micro-fabrication to control substrate architecture. Many studies have employed this technique to demonstrate how topographical changes can induce cellular pattern formation [113, 33, 63]. To further our understanding of the materials science tetrahedron, computational models

have been employed to synthesize existing measurements at the micrometer scale and provide mechanistic explanations for the topology-induced organization that has been observed experimentally. The desire to guide tissue assembly through manipulation of control variables such as substrate topology has provided a platform for efficient model parameter exploration and, more importantly, model validation.

A key feature of cardiovascular disease is cellular remodeling resulting in impaired contractile strength [111]. Two-dimensional studies are often employed to study contractility of tissue engineered structures since they are less computationally complex than three-dimensional studies yet yield insight into the experimental conditions that can recapitulate properties seen in native cardiac tissue. Biohybrid muscular thin films (MTFs) provide a route for studying contractile function of cultured cardiomyocytes while also bridging the gap between two- and three-dimensional systems [44, 4]. They incorporate various mechanical properties observed in a healthy myocardium as tunable parameters. To properly identify the impact of the various design parameters, free energy equations and finite-element modeling has been employed to study the deformation behavior in constrained cardiac muscular thin films [12]. This simulation tool allowed for the identification of material parameters that could be used to optimize fiber orientation in multi-layered patches for future implantation. This approach was later extended as a 3D phenomenological model that was more simplistic than previously proposed models yet captured both the active and passive behavior of unconstrained cardiac cells [110]. These techniques allowed the researchers to decouple MTF properties and study the nature of their interactions. By isolating specific parameters, they were able to predict how MTFs respond when mechanical properties are perturbed. From a systems biology point of view, these studies have helped researchers develop innovations to the heart-on-a-chip platform. This platform has been utilized to assess contractile stresses in diseased tissue as well as study the toxicity of nanomaterials [1, 2, 44, 54].

In native heart tissue, individual cells synchronize their beating rates so that the tissue

contracts in a rhythmic fashion. Synchronization occurs, in part, due to mechanical interactions between neighboring cells through intracellular gap junctions [127]. While isolated cardiomyocytes beat independently and spontaneously, synchronicity in beating rates may be observed when as few as two cells are grouped together [66, 61]. However, while it is known that the mechanosensitivity of cells plays a role in modulating beating rates, the mechanism that leads to a group of cells beating with regularity is not entirely understood. Focusing on the electrophysiological processes associated with contractions, beating frequency in a population of cells can be modeled using a small number of ordinary differential equations. Such models typically rely on equations describing electrical currents and action potentials such as Hodgkin-Huxley and Van der Pol equations. One approach explored the temporal behavior of synchronization by implementing a Markov chain process in conjunction with a deterministic Hodgkin-Huxley type model that had been previously proposed [138, 56]. This demonstrated that the time needed for synchronization depends on cell-cell conductance. In particular, when cell junctions are formed, a community effect is engaged whereby individual beating fluctuations decrease in favor of group stability. To explore the mechanism of synchronization stability in a network of pulsatile cells, a system of one-dimensional, interacting nonlinear oscillators was utilized [57]. It was shown that pairs of cardiomyocytes tend to beat synchronously with the cell that has a stable beating rhythm rather than the cell with the faster beating rate. This is an important consideration when dealing with a heterogeneous population of cardiomyocytes, as may be the case when performing pharmacological studies. Analyzing the properties of a complex system by manipulating the known properties of a smaller, simpler system is a common systems biology approach. This is emphasized by these synchronicity studies whereby researchers hope to take advantage of the community effect to control of a collection of cardiomyocytes with varying phenotypes, which may be indispensable to the development of therapeutic drugs [5, 145].

1.3 Modeling approaches at the cellular scale

Morphological changes resulting from heart disease have been shown to influence the geometry and resulting functionality of the individual cells that make up the cardiac tissue. Patients with ischemic cardiomyopathy, for example, have individual myocytes with significantly longer lengths compared to myocytes in healthy tissue [50]. Alterations in cellular geometry have been shown to influence the organization of internal structures such as the actin filaments and sarcomeres as well as impact cell contractility [97, 67, 131]. The ability of individual cells to self-assemble under different boundary conditions has been explored by using micro-contact printing to create individual cardiomyocytes of particular sizes and shapes. Some common shapes considered include square, rectangular, and circular geometries of varying sizes [97, 89]. In addition to boundary cues, cell morphology may be influenced by the physical properties of the substrate. Specifically, modification to substrate elastic moduli have been found to affect cell contraction rates, contractile strength, and myofibril organization [97, 58]. These changes may be linked to the cell's inability to adequately convert mechanical cues to chemical signals near the cell-substrate interface [10]. Such a process is regulated by an assortment of proteins collectively known as focal adhesions, suggesting the stability of these protein complexes are a key component in the contractile apparatus [26]. While experimental data has demonstrated that self-organization in cardiomyocytes can be induced through proper manipulation of boundary cues and substrate composition, computational models have provided insight into the exact nature of these interactions. Self-assembly can be enhanced or hindered by tunable parameters that may vary depending on cell type or morphology. Computational models are ideally suited for identifying these regulatory parameters and determining regimes which alter cytoskeletal dynamics in a way that optimizes self-assembly and contractility.

In a continuum model, several phenomena related to the cytoskeleton were coupled together [32]. This biochemical approach demonstrated the influence of cell shape on fiber orienta-

tion while simultaneously showing contractile forces decreasing when substrate rigidity was increased. A key outcome of the model is its ability to provide guidance for future experiments that aim to explore the cytoskeletal response to mechanical perturbations. As a simplification, this model did not consider focal adhesions, the anchoring sites for myofibrils which transmit mechanical cues between the cytoskeleton and the substrate. However, their dynamics were the central component to a phenomenological model that was developed to explore why focal adhesion proteins can be seen accumulating in the corners of stationary square cells [88]. Using deterministic integrin protein density equations linked to force generating stress fibers, the evolution of focal adhesion development was tracked. Allowing feedback between integrin clustering and force production was enough to produce the focal adhesion patterns observed experimentally. The model was validated using square fibroblasts and gave a mechanistic explanation for focal adhesion clustering in the corners of cells. Specifically, it predicted that integrin concentrations in the corners of the cell are increased because these high curvature regions allow stress fiber forces to be amplified. An extension of this model to cardiomyocytes of various cell shapes was later employed [54]. This deterministic model differed from previous approaches by incorporating myofibril maturation through pseudo-labeled integrin densities. The model demonstrated that myofibril length and parallel coupling work cooperatively to produce accurate focal adhesion localization and cell polarization for both homogeneous and heterogeneous boundary conditions. This work exemplifies the systems biology approach where the interplay between experiments and model construction is utilized to fit parameters, validate the model, make testable predictions, and generate new hypotheses for further studies.

The approaches described above either do not consider the elasticity of the substrate or treat it as a fixed parameter. However, since cells actively respond to variations in substrate composition [97], several computational models have been used to propose mechanisms that drive cell contractility in response to altered substrate rigidity. An early model was proposed to address how focal adhesion signaling events were linked to substrate elasticity [106]. In

this formulation, focal adhesions were treated as mechanosensors, represented as two harmonic springs in series, and it was assumed that signaling events were triggered once a sufficient amount of force had been built up in the focal adhesions. Doing so, researchers were able to demonstrate how the mechanical properties of the environment could regulate focal adhesion growth by varying the stiffness of the substrate. The two-spring model was later extended to allow for cell migration and proliferation in response to matrix elasticity changes [82]. In particular, the extended model predicts that cell migration is linked to the deformability of the substrate, where cells are more likely to migrate to regions that produce higher cellular stresses. These results have been built on and generalized by incorporated rate-dependent effects while simultaneously considering extracellular rigidity [14]. The one-dimensional phenomenological model used a three-spring configuration to predict the mechanosensing behavior of single cells. Specifically, the model allowed for time-dependent cellular response so that researchers could observe how the cell responds to step changes in substrate rigidity during migration. These studies have provided insight into how cell-material interactions regulate cellular response and growth. Specifically, these results can be used to develop scaffolds that may enhance tissue formation [6]. This demonstrates how interactions at one spatial scale can be used to influence dynamics at a larger scale, a core principle in understanding multi-scale problems via the systems biology approach.

1.4 Modeling approaches at the sub-cellular scale

A defining characteristic of the heart is that it undergoes consistent rhythmic contractions at the cellular (and tissue) scale. Cardiac muscle cells contain acto-myosin bundles consisting of myosin filaments crosslinked by α-actinin. These recurring clusters of proteins, referred to as z-bodies or z-bands, appear in regularly spaced intervals and mark the endpoints of the sarcomeres, the fundamental contractile units of myofibrils [28]. Optimal contractile

function occurs when sarcomere length is approximately 2 μm, but this can be disrupted by morphological changes like cell elongation due to cardiac hypertophy [77, 100]. When myofibrils are elongated, the initial increase in sarcomere length is followed by the addition of filaments and creation of new sarcomeres [100]. Despite returning the sarcomere length to its resting value, the elongated boundary leads to an increase in myofibril length and a decrease in cell contractility [67]. While numerous scaffolding proteins have been identified as potential instigators/regulators of the striation patterns [21, 45, 133], the mechanisms controlling self-assembly at this scale, including sarcomere addition and filament insertion, still remain elusive. Complicating matters is the challenge of visualizing pattern formation in early development. Despite these limitations, models of various forms have been proposed to address the formation of striations in myofibrils and the dynamics of actin filaments in the cytoskeleton.

The sequence of events that lead to the assembly of mature myofibrils has been outlined [28]. Briefly, sporadic clusters of α-actinin are observed on premyofibrils near the cell periphery. As maturation occurs, clusters on neighboring myofibrils align and striations are formed. Utilizing this observed sequence, a mechanical model was developed to explain the appearance of sarcomeric order in an initially unstriated bundle [47]. Investigators demonstrated the formation and coalescence of actin clusters via crosslinking and treadmilling of actin filaments. Assuming a collection of parallel actin and myosin filaments crosslink via physical interactions, spontaneous pattern formation occurred within their simulated bundle. Their approach suggested that cytoskeletal order may be obtained even without external scaffolding. While this approach demonstrated pattern formation within a single filament bundle, it did not consider how neighboring bundles might behave. Using a phase-order parameter, the degree of pattern alignment (registry) across neighboring myofibrils was modeled and quantified [31]. The researchers were also interested in the influence of this alignment on the cell's contractile function since changes in sarcomeric registry have been correlated with changes in substrate rigidity [74]. A key result was the ability to link z-band registration data

with contractile strain measurements in beating cells. This suggested that the beating of cardiac cells may be related to the registration of the cell's myofibrils. The study concluded that contractility could be optimized by appropriately altering the elasticity of the substrate. In this way, the beating of the cell, and hence the registration of z-bands in the cell, could be affected. Consequently, an optimal substrate stiffness may drive self-organization and registration within the cell. In the systems biology framework, these models primarily focus on making testable predictions. Dasbiswas and colleagues, for instance, based their model on experimental observations [74] and their conclusion was validated by the experimental findings of other researchers [97].

The cytoskeleton consists of a network of crosslinked actin filaments and provides shape and stability to cells. The mechanical properties of the cytoskeleton, and actin filaments in particular, have been well documented [70, 72]. However, some properties may be difficult to discover without hypotheses generated by computational models. For instance, a system of differential equations was constructed to investigate the role of actin polymerization in the distribution of filament lengths [40]. Using kinetic equations, the model provided insight into why the relative levels of actin and gelsolin monomers may lead to actin fiber length distributions that tend to be either exponential or reach a stable size distribution. Furthermore, the conditions under which interacting filaments would align, cluster or form filament bundles was explored. It was demonstrated that longer filaments were more likely to align into bundle-like structures while shorter filaments formed unaligned clusters, consistent with previous observations of actin networks crosslinked with α-actinin. The identification of several network behavior regimes provided a means through which actin polymerization could be manipulated to generate various types of crosslinked networks. This influenced future experiments related to fibrillization. The results for actin filament nucleation were lated used, for instance, to explore molecular mechanisms associated with neurodegenerative diseases [84]. This closes the experiment-model-experiment loop that is common in the systems biology methodology.

1.5 Multi-scale integrative modeling

An ongoing challenge in computational physiology is linking mathematical models across several spatial scales. While many of the models discussed in previous sections consider other physical scales implicitly, there is much to be gained by considering them explicitly. For instance, cardiac arrhythmias may occur due to a problem associated with the heart's electrophysiology. The complication is linked to the mishandling of electrical interactions by the individual cells that make up the contractile tissue. These electrical imbalances may be related to genetic mutations that cause alterations in ionic channels on the cell membrane [17]. In the systems biology sense, multi-scale modeling can be utilized to develop medical therapies on a patient-specific basis to target genetic abnormalities or mutations.

Since the interconnectivity of the heart can be studied in numerous ways, there is little restriction in how one might decide to couple scales together computationally. For instance, while it is difficult to obtain data of electrical and mechanical activity simultaneously at high resolution, it is possible to obtain insights into this link via multi-scale computational models. One such model considered the human ventricle as an organ-sized geometry with fiber-sheet architecture and employed an electromechanical approach that coupled membrane kinetics with a continuum mechanics model of the ventricles [59]. This approach allowed the researchers to study the influence of stretch-activated channel recruitment on fibrillation via alterations in channel conductance.

A notable mutliscale model was developed to understand the functional cues that guide tissue formation [140]. They combined a single cell model with a tissue level model and used finite element techniques to quantify cell deformations when subjected to mechanical load. This approach exemplifies a central component to multi-scale modeling techniques. Namely, the utilization and combination of models at individual scales that capture known phenomena while not exacerbating an already high computational cost. Several groups in the

cardiac modeling community have attempted to address this obstacle by developing advanced multi-scale simulators that combine, for instance, heart mechanics and electrophysiology [135, 126, 85]. Additionally, other fields have provided computational insights that have led to improved numerical schemes and reduced the computational expense that may be accrued when employing such methodologies [29].

1.6 Open questions

We have demonstrated that there are many different types of models that can be used to address questions that would be difficult to explore through experimentation alone. While there has been much progress afforded to experimentalists, many open questions remain from the genetics scale to the organ. Despite the abundance of information obtained from scaled models, synthesizing the data across the many layers of the heart has proven difficult. At the genetic level, an as-yet unresolved issue concerns how the failure of ionic channel inactivation can influence cellular polarization and lead to arrhythmogenesis [22, 87]. There is much interest in exploring how various ionic channels might have their function impeded as the result of genetic mutations [22]. How are proteins transcriptionally regulated and how do various genetic abnormalities influence protein structure? We know that there's an interdependence between various ionic channels [91] but how do these abnormalities influence mechanical and electrophysical properties at the organ level? Can we target protein functions at the subcellular scale to influence electrical activity at the organ scale? These question are a key driving force behind the development of drug therapies and computational modeling will be integral to guiding researchers towards effective intervention techniques.

In regards to the single cell level, it has been shown experimentally that native cardiomyocytes tend to exhibit a 7:1 aspect ratio [50, 49] and we have discussed different modeling approaches that explore why this aspect ratio may be ideal. Yet, how the optimal aspect

ratio is obtained in native cardiac tissue remains elusive. We also provided models that give insight into the events that influences myofibril alignment but it is still unclear how the various components work in concert to create the detailed architecture that is found in native cardiac cells. Currently, there is no consensus on whether the alignment within individual cells results from a top-down cascade, a bottom-up cascade, or even a middle-out cascade, all of which may be possible. This mystery is compounded when we compare myofibril alignment in immature and mature cardiomyocytes. Specifically, we do not yet know why immature and mature cardiomyocytes, subject to the same substrate and cell shape conditions, may produce substantially different organization in the central region of the cell [108]. This exemplifies the current gap in our understanding of stem cell differentiation and maturation *in vivo*.

The bidirectional influence of larger and smaller spatial scales has also not been resolved at the tissue level. Of particular interest at this scale is cellular and fiber orientation within cardiac tissue and how it may influence contractility. This has led to studies which consider not only the orientation of individual structures [119, 125] but also how multiple structures might be correlated with one another [34]. These studies have yielded several questions yet to be resolved: What are the dynamics of various correlated structures and how do they influence each other? If multiple constructs are not oriented correctly, how does that affect function? How can the observed correlations be used to enhance protocols for engineering tissue? Some of the models outlined previously were set up so that they can be extended in the future to address these questions.

While there are many open questions at the organ level, particular attention has been paid to analyzing the left ventricular wall. The left ventricle is a highly-organized structure with a smooth transition in fiber angle distribution, which has been used to identify different layers within the ventricular wall [118, 53]. This complication in myocardial fiber organization has limited our understanding of how the heart employs strain, torsion, and twisting to function

efficiently. For instance, we have not been able to properly explore layer-specific strain due in part to data acquisition constraints. This has also restricted our understanding of strain distribution patterns within the various layers and how it might influence global strain measurements. How these layers modulate their coordination and are able to distribute shear stress during contractions is still being explored both computationally and experimentally.

In addition to the modeling techniques discussed, several models use an optimization approach when describing the dynamics at the spatial scale of interest [134, 105]. This is often motivated by the observation that the heart structure appears to be organized in a mechanically optimal way [117]. Accordingly, it is not uncommon to find theoretical optimization approaches in computational models of the cardiac system. This invites its own sets of computational questions such as the types of optimization constraints that are appropriate for implementation as well as which energetic considerations accurately describe the energy transfer involved. The answers to these types of questions vary depending on the implementation procedure and problem of interest.

1.7 Conclusions

In order to understand the biological complexity of the heart, we must explore how the heart is structured and the physical processes that occur within each spatial scale. To accomplish this, structure-function relations are studied using *in vitro* models with the intent of recapitulating *in vivo* characteristics. Since the stiffness of the substrate has been shown to influence cellular development and contractility, a common approach to guiding assembly across the various hierarchical length scales is to adjust the properties of the ECM. This suggests that cardiac tissue structure and function can be altered by manipulating specific biochemical and mechanical processes. However, controlling these mechanical cues requires an understanding of the mechanism at play and how perturbations of that mechanism can

cascade bidirectionally in the spatial length scale.

A variety of computational models have been implemented to address this mechanism connectivity problem. In order for computational models to be effective, they must not only mimic experimental observations but also provide insight into the mechanism of interest. It is essential that they both mimic and predict experimental outcomes. This is especially important as a means of hypothesis generation since models allow for exploration of biological parameters and trends that may be time consuming or difficult to discover through experiments alone. While a powerful tool, due to the complexity of most biological systems, modeling requires assumptions and simplifications which can impact its effectiveness at generating testable hypotheses. Hence, an understanding of the system being modeled and what can meaningfully be reproduced and tested experimentally is critical.

The systems biology approach combines the strengths from both modeling and experimentation to provide a more complete view of the phenomena of interest. This is often exemplified by an experiment-model-experiment loop in which an observation drives the construction of a computational model which then generates a hypothesis that can be experimentally tested. This creates a positive feedback loop in which theoretical considerations and practical applications work in tandem to heighten our understanding of the mechanisms driving a biological system. This approach is especially useful when applied to the cardiac system since the heart is a complex multi-layered organ that coordinates its actions across multiple spatial and temporal scales. To tackle the problem requires a multi-pronged approach in which computational modeling provides insight into how mechanisms coordinate their efforts across length scales and experiments utilize those mechanistic links to develop functional tissue. This review can serve as a foundation for new researchers interested in using computational modeling to study the heart's emergent properties. We have highlighted some common modeling approaches within individual spatial scales and identified how each approach fits within the multi-scale dynamics of the heart. In this way, new computational

models may be built, and experiments proposed, to provide mechanistic explanations of how interactions within one of the hearts sub-systems affect the heart in its entirety.

Chapter 2

An adapted particle swarm optimization algorithm as a model for exploring premyofibril formation

[2]

2.1 Introduction

Across species, molecular interactions cause myofibrils to transmit forces both within and between neighboring myocytes with extreme precision, allowing for coordinated muscular contractions. This force transmission comes about because of synchronizing interactions across the highly ordered myofibril structure consisting of thick and thin filaments with α-actinin forming the mechanical link between thin actin filaments [11, 103]. Myofibrils form via a generalized process whereby each stage coincides with a specific collection of

[2]Reproduced from W. F. Sherman and A. Grosberg, 2020 AIP Advances 10:4 with permission from AIP Publishing

proteins, some of which can be used to track development from an immature to a mature state. Early stage myofibrils, termed premyofibrils, can be identified by the clusters of α-actinin distributed throughout their length [28, 103]. Following their formation, the spacing between these punctate α-actinin aggregates, designated as z-bodies, increases leading to α-actinin registration and lateral fusion amongst neighboring premyofibrils. This creates the striated patterns found on mature myofibrils referred to as z-lines [28]. These patterns have been observed in various cell types across multiple species including cardiac cells [76, 102], skeletal muscle cells [52, 133], and flight muscle cells [95, 90]. This corresponds to a basic organizational motif common to animals that use their muscles to produce force: the partition of the myofibril into repeating sarcomeres.

Since sarcomeres are the central contractile units of myofibrils in myocytes, much attention has been placed on tracking their formation, beginning with their myofibril precursors [11, 65]. However, despite sharing a similar overall pattern, different morphologies have been observed depending on the species of interest. For instance, not only is there a difference in initial z-body periodicity, there is also a difference in final sarcomere length. In mammalian cardiomyocytes, the distance between α-actinin clusters elongates from approximately $1.2\mu m$ for z-bodies to $2\mu m$ for mature z-lines [102, 74, 103] while in *Drosophila* flight muscle cells the distance increases from around $1.7\,\mu m$ to $3.2\,\mu m$ [95]. This growth has also been observed in the skeletal muscle of zebrafish though with different initial and final lengths [104]. However, the way in which the final sarcomere lengths are achieved in each species and muscle type is still unclear.

Sarcomerogenesis studies are typically framed with the assumption that there is a predetermined initial z-body pattern at the start of the maturation process [28, 103]. This is often claimed without reference to how α-actinin clusters self-organize into these punctate patterns. In fact, there is disagreement on whether proteins involved in maturation are also involved in the formation of z-bodies [76, 73]. Unfortunately, experiments focusing on early

protein coalescence in premyofibrils are scarce resulting in few proposals for exploring z-body pattern formation. This scarcity is due to the vast number of potential protein interactions that could be involved in early stage myofibrillogenesis, the exploration of which should not be undertaken blindly. Since theoretical models are well-suited for studying phenomena without emphasizing specific interactions, they may be key to addressing this unmet need and helping to guide future experiments.

In this work, we investigated whether α-actinin dynamics alone are sufficient to drive the self-organization of clusters into regularly spaced intervals simply through adjustments in individual protein activity. Specifically, we examined if α-actinin accumulation can be obtained in developing premyofibrils through an energy minimization mechanism without explicit reference to other proteins. Since the formation of premyofibrils has not been entirely explored, our approach may aid experimentalists in developing a roadmap for prospective studies of early stage myofibrillogenesis. By focusing on the recruitment and interactions between neighboring α-actinin clusters in different species and muscle cell types, our model can guide experimentalists towards identifying pattern-inducing factors associated with forming z-bodies. Once specific causal links are identified, exploration of the impact altered premyofibrils have on final sarcomere formation can be undertaken.

2.2 Results

Many studies have attempted to decode the complexities associated with the striated patterns found in mature muscle cells [11, 21, 90]. Often, emphasis is placed on the proteins involved in the transformation from premyofibrils with identifiable z-bodies into mature myofibrils with distinct z-lines [65, 103, 137]. However, this type of exploration does not address what causes α-actinin to form a pattern along premyofibrils in the first place. In an effort to gain insight into this phenomena, we viewed the cell as a mechanical operator which relies on an

efficient use of free energy to function including forming the premyofibril architecture. Our phenomenological approach focused on whether pattern formation could be induced without specific reference to other proteins that may be involved. This was investigated by employing a modified particle swarm optimization (PSO) algorithm that utilized the energetic profile of a swarm of α-actinin to guide z-body pattern formation.

2.2.1 Convergence of the adapted PSO algorithm

The standard PSO algorithm is a stochastic evolutionary algorithm with the ability to converge to a global optimum even when several local optima exist. To ensure proper convergence, many of the suggestions that have been put forth regarding the convergence of the standard PSO algorithm [139, 78, 42, 39] were integrated into the adapted PSO algorithm in this work. These include the incorporation of a dynamically adjusting inertia weight (Eq. (2.5)) into the velocity update rule [139], setting initial velocities to zero [42], and utilizing a swarm population size that is sufficiently large [39]. The implementation details and equations can be found in the Methods (Section 2.4).

The initial swarm resembled a collection of α-actinin randomly distributed throughout the simulated curve trajectory. Individual configurations were updated according to equations (2.4)-(2.8) with the possibility of cluster recruitment whenever the inter-cluster distance of the optimal swarm configuration was sufficiently large. Within each simulation, cluster accumulation can be viewed over the implemented time (Fig. 2.1A). Random initial swarms each tended towards a final configuration, converging before the maximum iteration counter $T_{\max}$ was reached (Fig. 2.1B). The swarm can be observed converging to the optimal swarm configuration with recruitment and movement mechanisms playing a key role in guiding algorithmic convergence. In particular, the final swarm configuration yielded an equilibrium inter-cluster distance near the ideal distance parameter, r_m, found in equa-

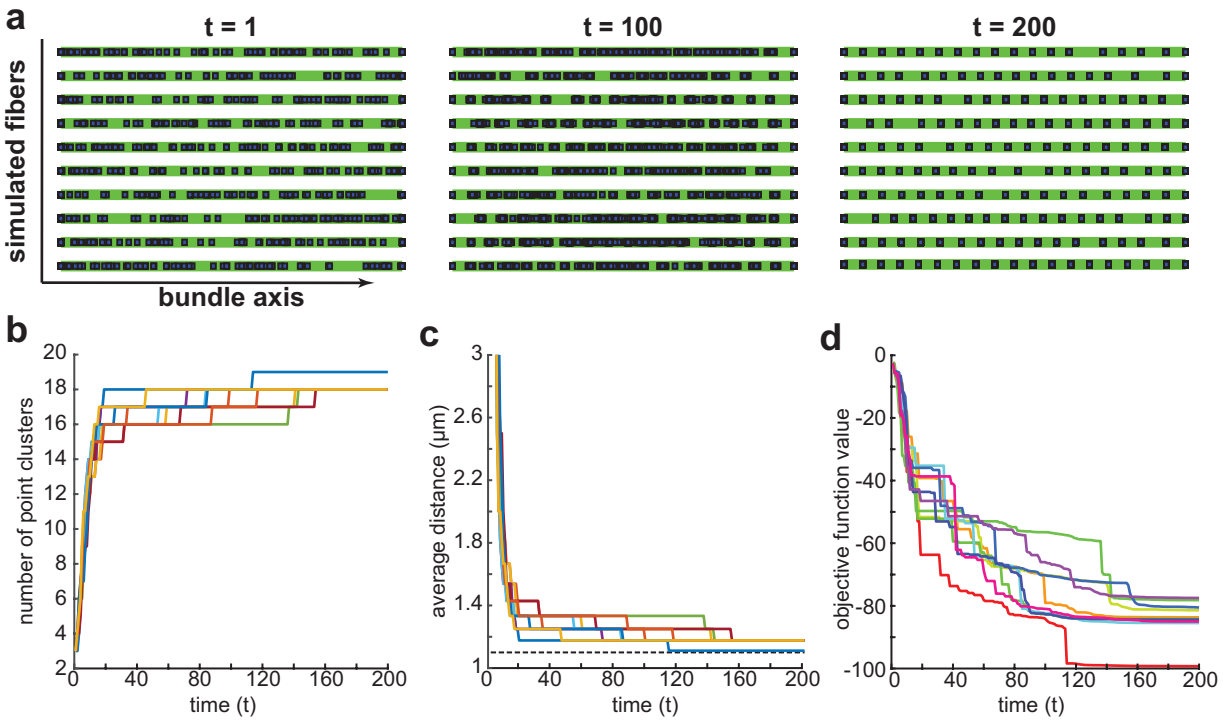

Figure 2.1. The adapted PSO algorithm converges to the optimal swarm configuration. (A) 10 simulations were run on a horizontal premyofibril (green) with $S = 60$ individual configurations in the swarm. Taken together, the swarm resembled a random distribution of α-actinin point clusters (blue). The clusters reached an equilibrium configuration as time increased from $t = 1$ to $t = 200$. (B) As the swarm evolved, new point clusters were incorporated into the swarm throughout all simulations (colors vary) until no new clusters could be added. (C) The inclusion of new clusters caused a decrease in the average inter-cluster distance for each simulation until it converged to a singular value, $r_m = 1.1\,\mu m$ (dotted line). (D) The injection of new point clusters corresponded to a decrease in the objective function value within each simulation.

tion (2.2) (Fig. 2.1B). The reduction in inter-cluster distance came about as a result of new clusters being recruited to the developing myofibril (Fig. 2.1C). The incorporation of new clusters into the swarm produced distinct reductions in the objective function value. Despite sharing a similar trend throughout all simulations, the objective function did not decay to a singular steady state value (Fig. 2.1D). Rather, the energy required to reach an optimal swarm configuration was dependent on the level of randomness and stochasticity in the initial swarm distribution. Many have speculated that cells function in ways which aim to optimize available free energy [24]. The possibility of an energy state transition occurring as a result

α-actinin recruitment invites speculation on the energetic nature of α-actinin modulation.

2.2.2 Pattern formation as determined by objective function parameters

A key observation of the convergence tests was the link between r_m and the convergence of the swarming algorithm, suggesting a correlation between the ideal distance value and the effective change in α-actinin mobility. Indeed, there are conflicting reports regarding the dynamic movement of α-actinin in the early stages of myofibril formation that coincide with muscle cell type [133, 76]. To explore if it is possible to generate patterns by manipulating α-actinin interactions and regulating binding affinity, the parameter pair governing the objective function were varied. Specifically, focus was placed on the ideal distance parameter r_m, which could coincide with muscle cell type, and the cluster searching distance d_{th}, which defined the necessary spatial distance for cluster recruitment to be considered.

In our simulations, the average inter-cluster distance is shown to be driven primarily by the ideal distance, r_m, and not by the recruitment searching distance, d_{th} (Fig. 2.2A). This is evident by the final inter-cluster distance converging to values near r_m despite changes to d_{th}. However, alterations in searching distance impacted the average uniformity of the resulting patterns (Fig. 2.2B). In particular, the appropriately chosen searching distance could increase uniformity levels for ideal distances larger than approximately $r_m = 1.25\,\mu m$. For ideal distances below this level, but larger than $r_m = 0.7\,\mu m$, the searching distance d_{th} would have little influence, as is evident from the consistent levels of uniformity that were seen. However, pattern formation begins to reduce for ideal distances smaller than $r_m = 0.7\,\mu m$ with the lowest levels occurring for searching distances below $d_{th} = 0.5\,\mu m$.

To further explore the influence of the ideal distance term r_m, the searching distance was fixed at $d_{th} = 0.5\,\mu m$ while r_m was allowed to vary. In this scenario, the final average

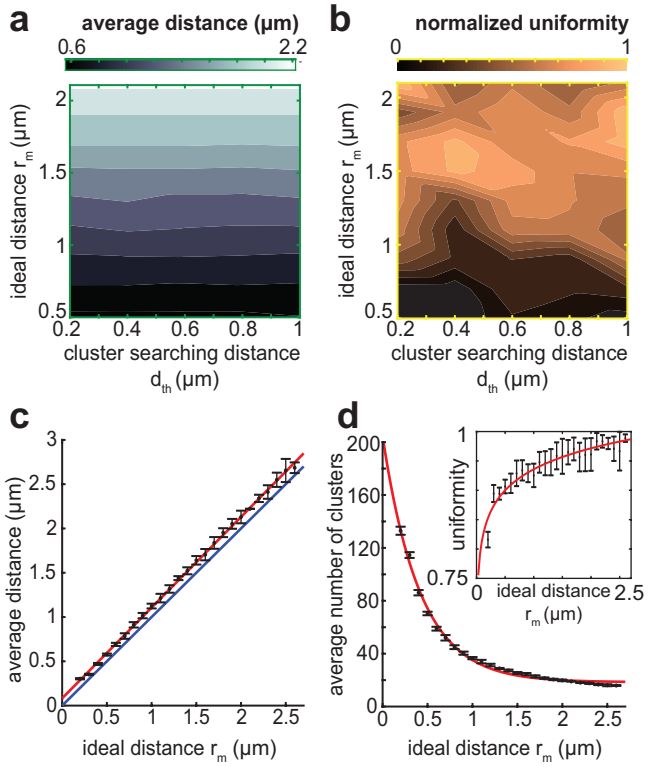

Figure 2.2. The ideal distance drives convergence behavior. (A) The average inter-cluster distance of the 10 fiber simulations showed a correlation between the convergence value and the ideal distance value r_m in the (d_{th}, r_m) parameter space. (B) The normalized uniformity measure viewed in the (d_{th}, r_m) plane revealed different pattern uniformities based on the location within the parameter space. (C) Fixing $d_{th} = 0.5\ \mu m$, the convergence values for each simulation (mean±SD) behaved linearly with varying r_m (red) with a convergence value always larger than r_m (blue). (D) The increase in ideal distance corresponded to a non-linear decrease in the number of clusters as well as a non-linear increase in uniformity (inset).

distance correlated with the changes in ideal distance in a linear fashion with consistently high levels of uniformity even at low r_m (Fig. 2.2C). Interestingly, the average distances consistently converged to values slightly larger than the specified ideal distance. Coinciding with the distance convergence, a clear link between average distance and number of final point clusters can be observed (Fig. 2.2D). However, while smaller distances yielded more point clusters, the relationship is nonlinear despite a constant searching distance. This appears to inversely mimic the nonlinear variation in the uniformity measure (Fig. 2.2D, inset), suggesting that uniformity may be more closely linked with the number of clusters

than with the final inter-cluster distance. This is a property that has been observed in mature myofibrils where increased uniformity appears to coincide with an uptick in the number of z-lines [21, 142]. Similarly, other properties of mature myofibrils such as sarcomeric length-regulation via specified proteins may have analogs in the immature case.

2.2.3 Impacts of myofibril shape on pattern initiation

Even though cells exist in a three dimensional environment, two dimensional experimental studies are often employed when studying myofibrillogensis [102, 96], leading to the discovery that premyofibrils first appear near the cell edge [28]. Despite their potential shape being restricted by the outline of the cell boundary, premyofibrils are often depicted as nearly straight curves with little to no variation in curvature [103]. This has inspired many researchers to model components of myofibrillogenesis using one dimensional reductions [47, 46]. One of the advantages of our approach is its adaptability into two dimensional studies without requiring large increases in complexity. This was used to investigate whether premyofibril shape was a potential influencer of either final inter-cluster distance or pattern uniformity.

Experiments from the literature emphasize premyofibrils that appear as long, slightly curved rods with distinct punctate patters. However, the patterns appear to degrade on curves closer to the cell edge, where premyofibrils have a larger radius of curvature [28, 96]. To explore this phenomenon, we applied our algorithm to two dimensional curves of varying lengths and curvatures. The curvature radius R_c was fixed at low ($20\ \mu m$), moderate ($56\ \mu m$), or high ($110 \mu m$) values and arc segments were constructed using fourth-order parametric Bézier curves with lengths L_c ranging from $20 \mu m$ to $60 \mu m$ (Fig. 2.3A). To perform our study, a linear transformation was applied that aligned the constructed curve with the horizontal axes. This allowed for lateral movement to be determined via equation (2.6) with the corresponding vertical coordinate being determined such that the resulting point cluster remained on the

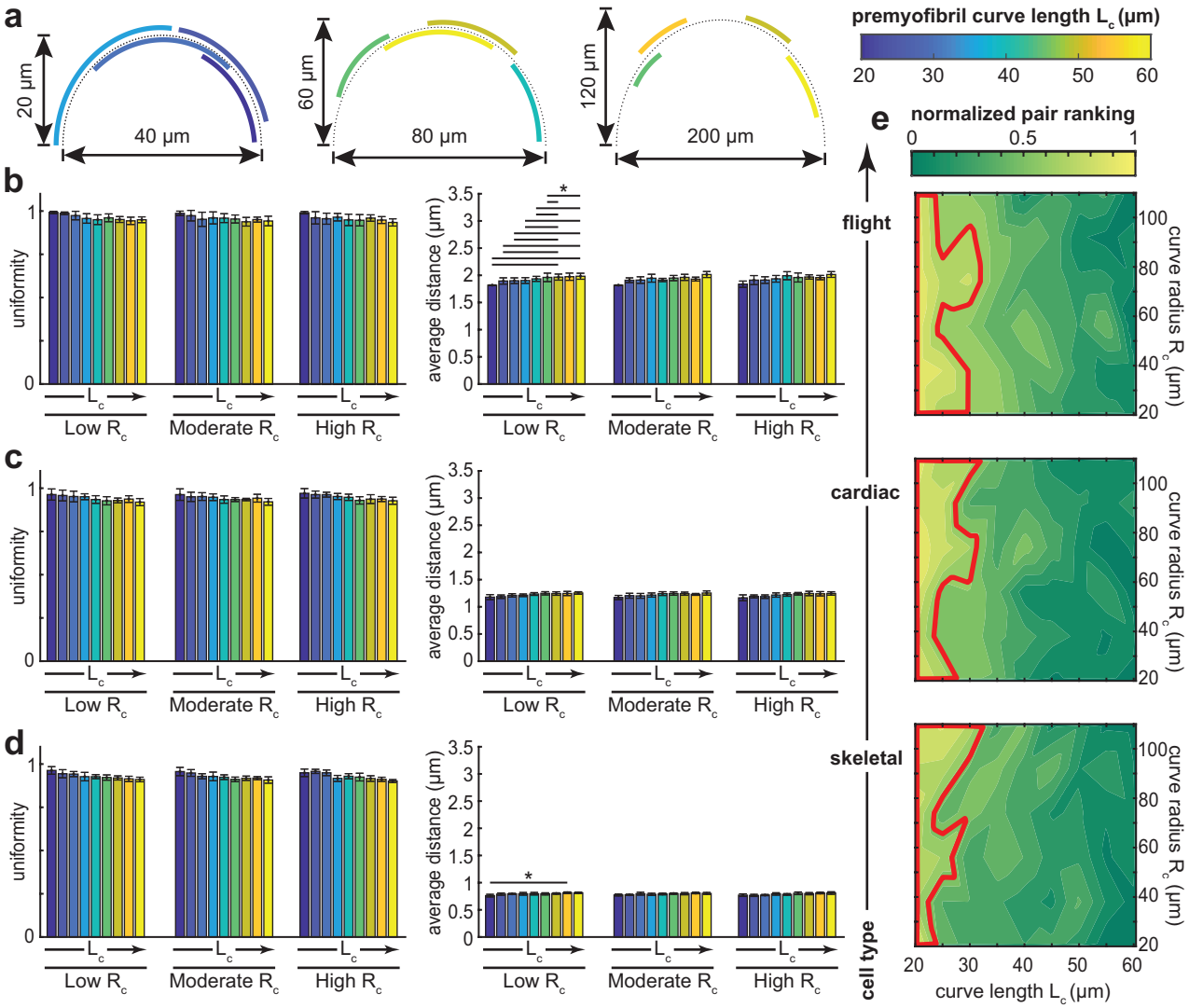

Figure 2.3. Curve shape influences pattern development. (A) Fourth order Bézier curves of various lengths (colorbar) were created for several types of curve radii including low ($20\,\mu m$), moderate ($56\,\mu m$), and high ($110\,\mu m$) values. (B)-(D) For low, moderate, and high curve radii, the curve lengths were varied and the resulting pattern was quantified according to uniformity (left plots) and average inter-cluster distance (right plots) as mean±SD for the 10 simulations. Pairings which demonstrated statistically significant differences ($p < 0.05$) were marked with a horizontal line. The simulations were performed using ideal distances corresponding to muscle cell type: $r_m = 1.8\,\mu m$ for flight muscle, $r_m = 1.1\,\mu m$ for cardiac muscle, and $r_m = 0.7$ for skeletal muscle. (E) For each muscle cell type, the ranking function (2.13) was employed and normalized in the L_c-R_c parameter space. The region with ranking value larger than the mean plus one standard deviation for the whole space is outlined (red).

transformed myofibril.

A common trend was seen in all three simulated muscle types (Fig. 2.3). High levels of uniformity were observed in all cases with no statistical differences found. However, there were differences observed in the final simulation distances at low curvature radius for the flight and skeletal muscle cell types. In the case of the flight muscle cell, the preassigned length of the myofibril appeared to play a role in the final pattern formation, with longer curves leading to larger deviations from the ideal distance (Fig. 2.3B). Interestingly, no significant differences were observed in cardiac cells, regardless of myofibril shape (Fig. 2.3C). However, the increase can also be seen when the shortest curve length is compared to one of the longer curve lengths in the skeletal muscle cell (Fig. 2.3D). As in the flight muscle, no statistically significant differences were observed at moderate or high radii of curvature in the skeletal muscle.

To further examine the link between these two fundamental characteristics, a parameter space exploration was employed (Fig. 2.3E). For each muscle cell type considered, myofibril curvature was altered and the resulting length-curvature pair was ranked based on how well the pattern balanced inter-cluster distances and uniformity (Eq. (2.13)). In general, increasing the curve length had a detrimental impact on the ranking when curvature radius was fixed. However, there was no consistency in the nature of this drop off. The highest ranked length-curvature pairs were identified in a cell-specific manner whereby equation (2.13) was employed throughout the parameter space and the region containing pairs with ranking larger than the mean plus one standard deviation were outlined. These high ranking regions differed in all muscle cell types yet none extended past the $\sim 33\,\mu m$ length marker. While flight cells contained two pronounced regions centered at low or moderately high curvatures, cardiac cells contained three protruding regions with high curvature included in the low and moderately high curvature radii. As the ideal distance reduced, two of these three regions shrank, prioritizing ranking towards straighter curves. Despite these distinct differences, the simulations did not produce any patterns containing an inter-cluster distance outside the ranges reported experimentally. Further exploring the impact of curve

shape on pattern initiation may yield insights into myofibrillogenesis. It is generally accepted that premyofibrils form near the cell periphery, which contain regions of high curvature in spreading cells, and move inwards during maturation [96, 28]. Prior to this spatial migration, the lengths and curvatures of the premyofibrils attempting to form in these regions may be subjected to shape constraints that play a vital role in guiding α-actinin recruitment and clustering.

2.2.4 Self-organization may be guided by group behavior

As of yet, a unifying mechanism that guides self-organization across multiple species has not been identified. There is speculation, however, that the variability found in the observed patterns may point towards fundamental differences in protein behavior which are species-specific. Indeed, there has been some evidence that α-actinin behavior may be altered through interactions with various regulatory, signaling, and metabolic proteins [13, 114]. The methods by which these regulatory interactions are entrenched in some developing cells are not entirely known but they may be linked to key differences present in different cell types [81]. To explore these potential influencers in our model, cluster behavior profiles were altered by manipulating two acceleration parameters: an individualized cognitive coefficient c_1 which biases behavior towards the best solution for the specific individual and a group social coefficient c_2 that biases behavior towards the best solution for the swarm. Typically, these values lie in the range $0 \leq c_1, c_2 \leq 4$ with large values indicating quick movement towards the target goal [78]. The prescribed behavior profiles influence individual trajectories with $c_1 > c_2$ indicating a preference towards optimizing individualized self-learning behavior while $c_1 < c_2$ prioritizes optimization based on group behavior.

To examine the influence of biasing behavior on final pattern formation, the pair of acceleration parameters were varied within the range suggested by the literature [78]. The simulated

myofibril was given a curve length of approximately 35 μm and radius of curvature 40 μm, a shape combination which previously fell outside of the highest ranked regions for each muscle cell type (Fig. 2.3E). Using the ranking function, the regions with the highest ranked parameter pairs were identified for each muscle cell type within the parameter phase space (Fig. 2.4A). The behavior pairing with the largest overall ranking for each cell type were identified and found to be clustered near each other. Often, each behavior type is assumed to have an equal level of influence [78] but such pairings were not optimal for any of the cell types simulated. Interestingly, all highly ranked pairs had a group coefficient c_2 above unity but this property was not observed with the self-learning coefficient c_1. As might be expected, there was no region common to all three muscle types but a transitory area could be identified whereby the different muscle types could be simulated with minimal parameter variation (Fig. 2.4A). Biologically, these observations imply that α-actinin may behave differently depending on muscle cell type. In fact, there is evidence of genetic variability in the different α-actinin isoforms in multiple species [81]. Whether this variability is linked to alterations in α-actinin mobility or binding affinity has not been determined.

To further analyze the influence of variations in α-actinin behavior, we explored the convergence behavior within the simulations. The regions with highest rank appeared to correlate with the behavior pairings that produced patterns with minimal deviation from the idealized distance value (Fig. 2.4B-2.4D). For skeletal muscle, all parameter pairs yielded average distance values that were within the range of values previously reported. However, that was not the case for the other two muscle types. In the cardiac simulations, inaccurate patterns were produced when self-learning was highly favored over socialization (Fig. 2.4C) while for flight muscle, the lack of group interactions ($c_2 = 0$) prevented the formation of valid patterns (Fig. 2.4D). This suggests a possible correlation between the idealized distance value r_m and the size of the valid parameter pairings as increases in r_m corresponded to a shrinkage of the potential parameter space (Fig. 2.4E). This may support the hypothesis that the level of influence different proteins have on α-actinin behavior, and the resulting pattern, may

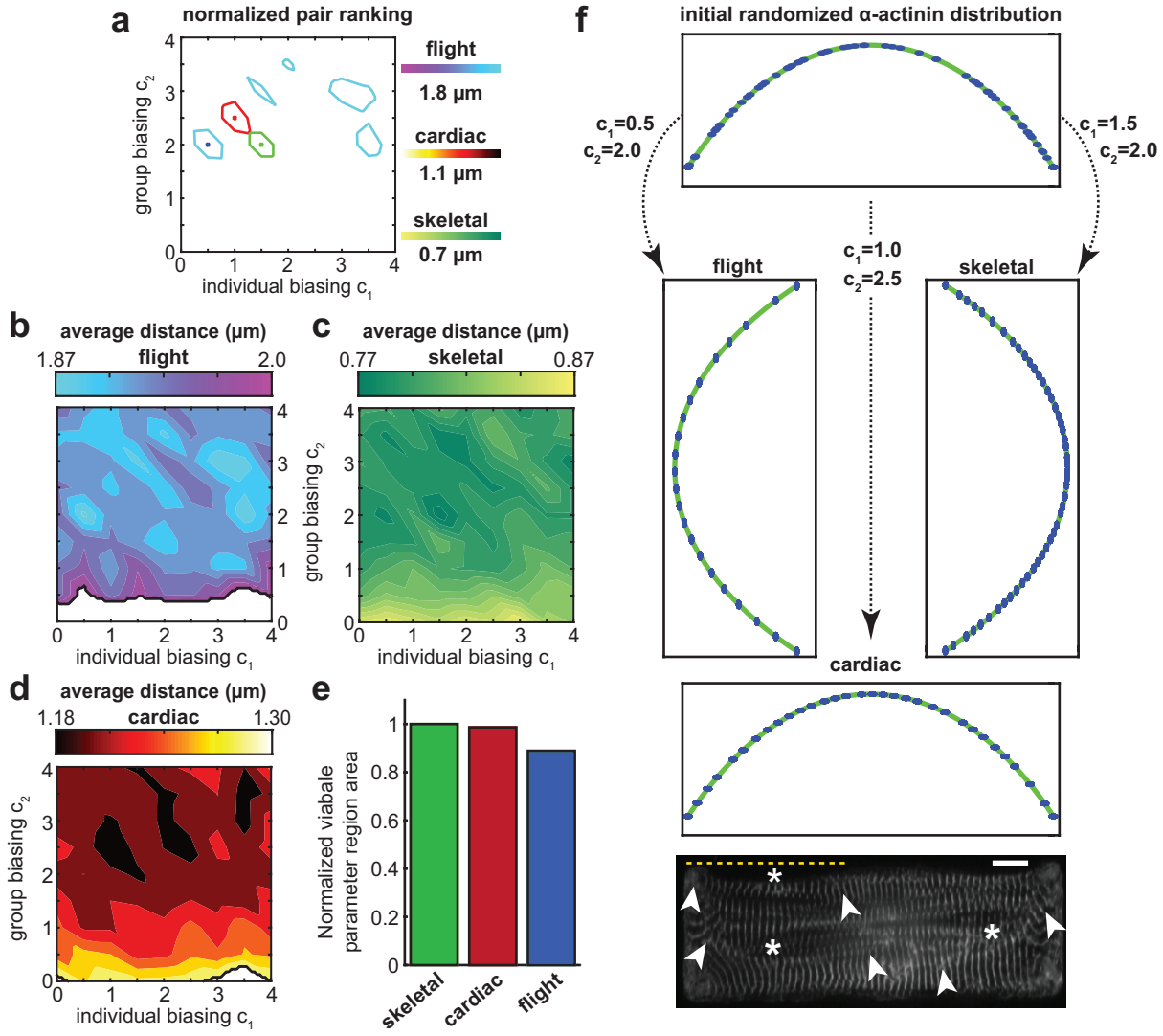

Figure 2.4. The choice of biasing parameters dictates the equilibrium pattern. (A) The individual (c_1) and group (c_2) biasing behavior parameters were varied for each muscle cell type simulated. The ranking function (2.13) was normalized and all regions with values larger than 0.56 were outlined for flight (blue), cardiac (red), and skeletal (green) muscle. (B)-(D) The average inter-cluster distance for each simulated cell type was plotted in the (c_1, c_2) parameter space with blank regions indicating parameter pairs that yielded average inter-cluster distance values outside the range observed experimentally. (E) The area of the parameter space region that yielded biologically relevant patterns was calculated and normalized relative to the area of the entire parameter space for each simulated muscle cell type. (F) From a common initial α-actinin distribution, the choice of biasing parameters can produce patterns for each muscle cell type. These are consistent with experimental data such as neonatal rat ventricular cardiomyocytes with z-lines identified by α-actinin staining. Curved myofibrils are identified by an asterisk with arrowheads identifying the myofibril trajectory. A yellow dotted line is provided for visual reference of a horizontal line. Scale bar: 10 μm.

vary according to cell or species type [81]. In any case, in all three cell types considered, it was possible to obtain a final distribution with average inter-cluster distance near the ideal distance that utilized both self-learning and group biasing ($c_1, c_2 \geq 1$). However, doing so could result in distributions with impaired uniformity. While some high ranking regions could be found for each cell type when individual behavior was prioritized ($c_1 > c_2$), more high ranking regions were produced when emphasis was placed on group behavior ($c_2 > c_1$), suggesting that the ability for α-actinin to interact with neighboring proteins is essential for pattern formation.

Fig. 2.4A illustrates how α-actinin dynamics can be modulated in order to form various punctate configurations. The experimentally observed patterns could be recreated through the appropriate choice of biasing parameters. Specifically, within each high ranking region, the parameter pairs that yielded the highest ranking values were chosen to demonstrate how premyofibril assembly may differ in different cell types (Fig. 2.4F). Starting with an initially random distribution, each pair of biasing parameters were implemented and the final α-actinin distributions were obtained. These distributions produced patterns which had high levels of uniformity and average inter-cluster distances that resembled the values found in the literature. Movement towards different parameter space regimes may come about by modulating protein interactions. This may be done in a species- or cell-specific manner, prompting further analysis of the interactions that allow each cell type to uniquely regulate protein behavior.

2.3 Discussion

There are many aspects regarding the dynamics governing myofibrillogensis that remain unresolved. In most studies, emphasis is placed on the proteins affiliated with the transition from z-bodies to z-lines following the identification of fully formed premyofibrils. However,

there is currently no consensus on how such a structure is formed. To aid experimentalists in this endeavor, we constructed a modified PSO algorithm and demonstrated that it may be possible to generate experimentally observed patterns through manipulation of the underlying mobility, recruitment and binding dynamics of α-actinin. By utilizing energy-state transitions and allowing for premyofibrils of various lengths and radii of curvature, we were able to explore how relations such as curve shape and biasing behavior may influence the formation of α-actinin patterns.

Since the sarcomere is the central contractile unit in a myofibril, many theoretical and experimental models concerned with sarcomeric organization are built on the view that self-organization comes about due to tension-mediated interactions between actin and myosin filaments [47, 136, 30]. While these models accurately display tension as an important factor in guiding maturation, they often ignore the central role α-actinin plays in z-body formation. Our approach differs by emphasizing α-actinin dynamics which has been shown to display differences in mobility depending on the muscle cell type [133, 76]. While other models have not attempted to recreate this property, we were able to mimic this response by considering different behavior profiles. Additionally, previous models favored one dimensional simplifications [46, 47] whereas our approach allows for two dimensional studies with minimal additions. Experimental data obtained from 2D cultures are commonly used and have demonstrated complex cytoskeletal networks consisting of myofibrils with varying curvatures [28, 46]. Previous models have not been set up to address how this factor influences premyofibril formation while our model allows for the inclusion of curve shape considerations. Since muscle cells *in vivo* are cylindrical in shape [71], it is possible that the 3D structure of developing myofibrils may influence pattern formation [7]. Several studies have attempted to decode the complex 3D structure that appears in the later stages of myofibril maturation, referred to as the z-disk [103, 102, 43]. However, given the increase in experimental complexity associated with developing 3D cultures [7, 38], two dimensional computational studies such as ours provide a basis for hypothesis testing with the possibility for extensions

in the future. Future extensions of our approach would include three dimensional studies whereby the given premyofibril can have planar curvature as the result of rotations into the z-axis. This additional degree of spatial freedom may be included directly, allowing for three dimensional visualization, or indirectly where a three dimensional curve can be projected onto a two dimensional plane.

Our model proposes that premyofibrils can be influenced towards developing different punctate patterns by altering the behavior of individual α-actinin molecules. In the same way that a list of maturation-affiliated proteins has been assembled [103], our results highlight how a catalog of α-actinin influencers in developing premyofibrils also needs to be compiled. One such influencer that has already been discovered in eukaryotic cells is cofilin. This protein has been shown to increase the cross-linking of actin filaments by increasing the number of potential α-actinin binding sites [13]. Such an influence would correspond to a change in the biasing parameters in our model (represented by c_1 and c_2). It is possible that the dynamics governing this increase in binding sites is linked to the changes in mobility in different muscle cell types but this has yet to be examined.

Based on our framework, our model suggests that experiments focusing on the sequence of events leading to premyofibril formation prioritize the nature of initial α-actinin recruitment and its relation to the scaffolding proteins that bind to actin filaments. There is already evidence that proteins such as N-RAP interact with actin filaments prior to the recruitment of α-actinin but do not appear to drive sarcomere formation [76, 73]. These types of proteins may be linked to our cluster searching distance d_{th}, influencing α-actinin recruitment dynamics and eventual pattern formation. Additionally, the current model can be used as a building block towards linking the formation of α-actinin z-bodies with the known interactions that occur during maturation. Experimentalists can use our phenomenological findings to inform their explorations of the dynamics that are at play during the early stages of myofibrillogenesis. By emphasizing the dynamics of α-actinin, our model can be extended to

include additional cell types not considered here such as vertebrate smooth muscle. Smooth muscle cells contain α-actinin z-bodies but have a different contractile mechanism than striated muscle cells [18]. This exemplifies how exploring initial α-actinin pattern formation phenomenologically may be advantageous from a modeling perspective as it allows for a discussion of general characteristics that may be applicable to many different cell types.

2.4 Materials and Methods

The PSO algorithm is a population-based algorithm inspired by the social behavior observed in bird flocks and fish colonies [78]. A key component of this algorithm is its ability to use local interactions between neighboring bodies to influence global behavior in service of optimizing a prescribed objective function. In our formulation, a swarm refers to a collection of α-actinin cluster configurations, each of which may form as the result of an accumulation of α-actinin proteins along the simulated myofibril. The α-actinin distribution for each configuration was then updated iteratively by optimizing the objective function, as outlined in Fig. 2.5.

2.4.1 Energy-based objective function

We constructed an objective function that utilized inter-cluster distance within a configuration and accounted for the energetic cost-benefit of adding clusters to each configuration. Newly added clusters allowed the swarm to consider different configurations where a new state was adopted if it was energetically favorable. Assuming a collection of N clusters with locations $\mathbf{r}_1, \ldots, \mathbf{r}_N$ within a given configuration, we wrote the objective function at iteration

t as

$$f(\mathbf{r}_1, \ldots, \mathbf{r}_N) = \sum_{i<j} V(r_{ij}) + \sum_{k=1}^{K_l} E_k \delta_k, \tag{2.1}$$

where the first sum denoted the energetic cost of maintaining the swarm in the current state and the second sum denoted the energetic cost-benefit of adding new α-actinin clusters to the current swarm.

The potential energy function V was chosen under the assumption that α-actinin clusters aim to achieve an optimal distance from neighboring clusters, as has been reported experimentally [74, 103]. This behavior is adequately captured by the Lennard-Jones potential energy function

$$V(r_{ij}) = \epsilon \left[\left(\frac{r_m}{r_{ij}} \right)^{12} - 2 \left(\frac{r_m}{r_{ij}} \right)^{6} \right], \tag{2.2}$$

where the strength of the cluster interactions is dependent on the inter-cluster distance $r_{ij} = |\mathbf{r}_i - \mathbf{r}_j|$, ϵ denotes the depth of the potential energy well, and r_m denotes the ideal equilibrium inter-cluster distance. In the second summation, K_l denotes the number of potential clusters that could be added to the swarm with E_k denoting the energetic cost-benefit of incorporating a new cluster $\mathbf{s}_k$ to the swarm configuration. The step function δ_k indicates whether adding $\mathbf{s}_k$ is energetically favorable.

2.4.2 Energetic cost-benefit function

To incorporate a new α-actinin cluster $\mathbf{s}_k$ into a configuration, both the current optimal swarm configuration $\{\mathbf{r}_1, \ldots, \mathbf{r}_N\}$ and the newly incorporated clusters $\{\mathbf{s}_1, \ldots, \mathbf{s}_m\}$ where $m < k$ were considered. To this end, we wrote $X = \{(\tilde{\mathbf{r}}_0, \tilde{\mathbf{r}}_1), (\tilde{\mathbf{r}}_1, \tilde{\mathbf{r}}_2), \ldots, (\tilde{\mathbf{r}}_N, \tilde{\mathbf{r}}_{N+1})\}$ where $\mathbf{r}_0$ and $\mathbf{r}_{N+1}$ denoted the two endpoints of the myofibril and $\tilde{\mathbf{r}}_i \in \{T\mathbf{r}_0, \ldots, T\mathbf{r}_{N+1}\}$ with

$\tilde{\mathbf{r}}_{i,x} < \tilde{\mathbf{r}}_{i+1,x}$. The linear transformation T aligned the myofibril of interest with the x-axis so that a pseudo-ordering of the clusters could be created. We then defined E_k as

$$E_k = \sum_{(\mathbf{x}_1,\mathbf{x}_2)\in X} P(\mathbf{s}_k, \mathbf{x}_1, \mathbf{x}_2) \left[\sum_{j=1}^{N} V(|\mathbf{s}_k - \mathbf{r}_j|) + \sum_{m<k} V(|\mathbf{s}_k - \mathbf{s}_m|)\delta_m \right], \tag{2.3}$$

with

$$P(\mathbf{s}_k, \mathbf{x}_1, \mathbf{x}_2) = \begin{cases} 1 & (T\mathbf{s}_k)_x \in (\mathbf{x}_{1,x}, \mathbf{x}_{2,x}) \\ & \quad \text{and } (T\mathbf{s}_m)_x \notin (\mathbf{x}_{1,x}, \mathbf{x}_{2,x}) \text{ for } m < k \\ 0 & \text{otherwise} \end{cases} .$$

The first summation within the brackets considers how a newly proposed cluster would influence the current optimal configuration while the second summation incorporates the influence of clusters which have already been proposed. The outer summation and the function P restricts only one cluster to be added to a myofibril segment per iteration.

2.4.3 Algorithm overview

Full implementation was achieved by using a three step process. Following initialization, configurations within the swarm were updated using position and velocity equations common to standard PSO algorithms, as described below (Fig. 2.5, green box). Once new configurations were proposed, the simulated myofibril was segmented into potential α-actinin recruitment zones whereby an energy state transition could occur (Fig. 2.5, blue box). This process was repeated until the maximum number of iterations $T_{\max}$ was reached. The final configurations were then analyzed for pattern formation and consistency (Fig. 2.5, pink box).

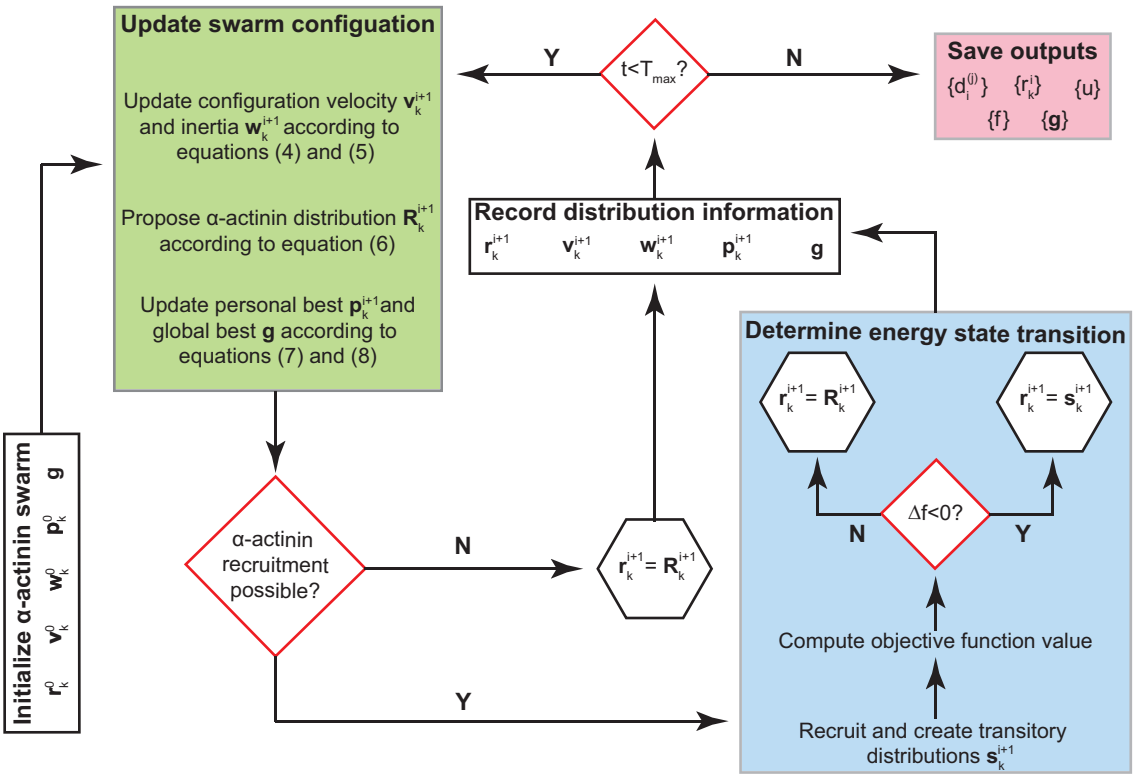

Figure 2.5. Overview of the adapted PSO algorithm. Following initialization, the algorithm can be broken down into two main components: the position- and velocity-related update equations (green box, described in Section 2.4.3) and the integrated energy state transition process (blue box, described in Section 2.4.3).

Initialization

The swarm was initialized by specifying a swarm size S and assuming there was initially one cluster on either end of the myofibril curve and one cluster placed randomly within the curve per configuration. The algorithmic variables were initialized by assuming each cluster initially had zero velocity and was in its locally optimal configuration: $\mathbf{v}_k = 0$ and $\mathbf{p}_k = \mathbf{r}_k$ for all $k = 1, \ldots, S$. The optimal configuration for the swarm was initially set to be the most energetically favorable of all the individual configurations: $\mathbf{g} = \mathbf{r}_k$ such that $f(\mathbf{r}_k) \leq f(\mathbf{r}_j)$ for all $j = 1, \ldots, S$.

Configuration updates

While $t < T_{\max}$, all algorithmic variables were updated according to the following rules:

1. For $k = 1, \ldots, S$, $\mathbf{v}_k$ was updated using

$$\mathbf{v}_k(t + \Delta t) \quad = \quad \omega(t)\mathbf{v}_k(t) + \mathbf{R}_1 c_1(\mathbf{p}_k - \mathbf{r}_k(t)) + \mathbf{R}_2 c_2(\mathbf{g} - \mathbf{r}_k(t)). \tag{2.4}$$

   The parameters $\mathbf{R}_1$ and $\mathbf{R}_2$ were random values chosen from a uniform distribution while c_1 and c_2 denoted scalar weights that bias the attraction towards $\mathbf{p}_k$ and $\mathbf{g}$. The inertial parameter ω dynamically adjusted at each iteration via the relation

$$\omega(t) = \omega_{\max} - (\omega_{\max} - \omega_{\min})\frac{t}{T_{\max}}, \tag{2.5}$$

   where $\omega_{\min}$ was the final value of ω and $\omega_{\max}$ was the initial value of ω, typically taken near 1 [78].

2. For $k = 1, \ldots, S$, $\mathbf{r}_k$ was updated using

$$\mathbf{r}_k(t + \Delta t) = \mathbf{r}_k(t) + \mathbf{v}_k(t + \Delta t)\Delta t. \tag{2.6}$$

3. For $k = 1, \ldots, S$, $\mathbf{p}_k$ and $\mathbf{g}$ were updated using

$$\mathbf{p}_k(t + \Delta t) = \begin{cases} \mathbf{p}_k(t) & f(\mathbf{r}_k(t + \Delta t)) \geq f(\mathbf{p}_k(t)) \\ \mathbf{r}_k(t + \Delta t) & f(\mathbf{r}_k(t + \Delta t)) < f(\mathbf{p}_k(t)) \end{cases} \tag{2.7}$$

   and

$$\mathbf{g} = \mathbf{r}_k(t + \Delta t) \tag{2.8}$$

such that $f(\mathbf{r}_k(t+\Delta t)) \leq f(\mathbf{r}_j(t+\Delta t))$ for all $j = 1, \ldots, S$.

Energy state transition

After new configurations were obtained, we determined if the swarm should undergo a state transition by adding new clusters. If the distance between neighboring clusters in the optimal swarm configuration was larger than the minimum required segment length d_{th}, then new clusters could be incorporated randomly onto the myofibril segment between them. A newly suggested cluster $\mathbf{s}_k$ was accepted into the swarm if its inclusion would result in a reduction of the objective function value, $\Delta f < 0$. Once a new cluster point within a myofibril segment was accepted into the optimal swarm configuration, a corresponding local cluster $\mathbf{r}$ was randomly placed within the same myofibril segment for each individual configuration. Each of these new local clusters were initialized using the same requirements as before: $\mathbf{p} = \mathbf{r}$ and $\mathbf{v} = 0$.

Within each simulation, we allowed for movement in one dimension of each cluster to be determined by the algorithm and required the corresponding second dimension to be chosen such that the cluster remained on the given myofibril curve. We also required $\mathbf{r}_k$ to always be confined within the designated boundaries by enforcing absorbing boundary conditions: If $\mathbf{r}_k$ was predicted to move a cluster beyond the boundary, then the cluster was reset to the boundary and its velocity was reset to 0.

2.4.4 Distance, uniformity and ranking measurements

Average inter-cluster distance

For pseudo-ordered cluster points $\{\mathbf{x}_1, \ldots, \mathbf{x}_N\}$ in the jth configuration ($1 \leq j \leq S$), the inter-cluster distance between clusters $\mathbf{x}_i$ and $\mathbf{x}_{i+1}$ was defined as $d_i^{(j)} = |\mathbf{x}_i - \mathbf{x}_{i+1}|$.

The average distance within simulation number s_k was $\overline{d}_{s_k} = (1/S)\sum_j \overline{d}_i^{(j)}$, where $\overline{d}_i^{(j)} = (1/N)\sum_i d_i^{(j)}$ was the average distance of the clusters located at $\{\mathbf{x}_1, \ldots, \mathbf{x}_N\}$. Given N_{sim} simulations, the average inter-cluster distance of the swarming algorithm was

$$\overline{d} = \frac{1}{N_{\text{sim}}} \sum_{s_k} \overline{d}_{s_k}. \tag{2.9}$$

To aid in parameter space exploration whereby a pair of parameters (p_1, p_2) were varied, the average inter-cluster distance of the swarming algorithm was rescaled relative to the ideal distance r_m,

$$\overline{d}_T(p_1, p_2) = \frac{\overline{d}(p_1, p_2) - r_m}{\max_{(q_1,q_2)} |\overline{d}(q_1, q_2) - r_m|}. \tag{2.10}$$

Uniformity

To determine whether the point clusters were uniformly distributed, an adjusted coefficient of variation (COV) measure was utilized. To this end, the minimum distance between point $\mathbf{x}_i$ and all other points was first determined: $\gamma_i = \min_{j \neq i} |\mathbf{x}_i - \mathbf{x}_j|$. The uniformity measure was then defined as

$$u = \frac{1}{\lambda_{\text{rand}}} \left[\lambda_{\text{rand}} - \lambda\right], \tag{2.11}$$

where $\overline{\gamma} = (1/N)\sum_i \gamma_i$ and $\lambda = (1/\overline{\gamma})\left[(1/N)\sum_i (\gamma_i - \overline{\gamma})^2\right]^{1/2}$, a common COV measure of uniformity. The parameter λ_{rand} denotes the maximum uniformity measure that may occur from 60 simulations of N randomly distributed points along the simulated myofibril. By including this parameter, the uniformity measure was expected to range from zero to unity with $u = 1$ corresponding to a uniformly distributed collection of points. As with the inter-cluster distance measurements, for each simulation s_k the average uniformity was denoted $\overline{u}_{s_k}$ and the average uniformity of the swarming algorithm was defined as the average uniformity

over all simulations:

$$\overline{u} = \frac{1}{N_{\text{sim}}} \sum_{s_k} \overline{u}_{s_k}. \tag{2.12}$$

Ranking function

To determine the influence of a pair of parameters (p_1, p_2) on the behavior of the resulting configuration, a ranking function was constructed which utilized the average inter-cluster distance and uniformity measurements. For each parameter pairing, the distance measurement (2.10) was normalized and rescaled to prioritize values closer to zero and penalize values away from zero, regardless of whether they deviated towards the positive or negative ends of the spectrum. Thus, the ranking function was defined as the product of the average uniformity and the prioritized distance function:

$$R(p_1, p_2) = \overline{u}(p_1, p_2) \cdot \exp\left[-\frac{\overline{d}(p_1, p_2)^2}{2\sigma^2}\right], \tag{2.13}$$

where σ is the standard deviation of the collection of parameter-generated distances $\{\overline{d}_T\}_{(p_1,p_2)}$.

2.4.5 Statistical analysis

Simulation data, when applicable, was expressed using the mean with error bars representing the standard deviation. Statistical significance between data groups was determined using one-way analysis of variance followed by the Tukey-Kramer post-hoc test for pairwise comparisons. A p-value less than 0.05 was considered statistically significant.

Chapter 3

A dynamic energy minimization model for cytoskeletal organization

[3]

3.1 Introduction

A healthy heart is able to regulate its complex dynamics due to its organized, hierarchical structure [108, 41]. In diseased hearts, this high degree of organization is inhibited with many physiological and structural properties appearing compromised [69, 25, 51]. For instance, cardiomyocytes from diseased hearts exhibit changes in cell size and shape [107]. In isolated cardiomyocytes, cell shape changes have been associated with inhibited cell contractility and reduced sarcomeric registration [50]. To study whether there is a link between the altered cellular structure and the inhibited function of cardiomyocytes, engineered tissue capable of recapitulating the phenomenological properties found in maladaptive cardiac tissue must

[3] W. F. Sherman, M. Asad and A. Grosberg, submitted 2020 PLOS Comput Biol

be developed. One such property is the organization of the cytoskeleton at different length scales. For example, cardiac tissue may be globally isotopic while being locally anisotropic [36]. Controlling this balance in organization at the global and local scales is an ongoing challenge. Spatial constraints further complicate matters as myofibrils are multidimensional constructs and need to compete for space in a densely packed environment [9]. As a result, individual cells may contain myofibrils with vastly different lengths, curvatures and locations, in some cases even having their placement impacted by the presence of the nucleus [131]. Each of these factors contributes to the challenge of mimicking cytoskeletal organization in engineered tissue. The development of computational models capable of recapitulating these observed behaviors may serve as an invaluable tool. Modeling provides a means for efficiently exploring these characteristics and may lead to better control of the cytoskeletal architecture *in vitro*.

Numerous theoretical models have been employed to address how cytoskeletal organization might be obtained, as has been recently reviewed [109]. Kassianidoua et al. explored how the cytoskeletal architecture was related to stress fiber mechanics using a minimalistic active cable network model [62]. They considered how stress fiber connections could influence individual stress fiber mechanics. However, the model did not address the influence of cell geometry on fiber shape and only considered a small, simplified portion of the cytoskeletal network. Yuan et al. produced a model that allowed for the geometry of the cell to be included and predicted the mechanical stress in the cytoskeleton [144]. By including the dynamics of focal adhesions, the collection of proteins that anchor the cell to the substrate, they were able to predict the myofibril-associated principle stress direction in both regular and irregularly shaped cells. This model did not consider spatial constraints that would cause a myofibril to interact with neighboring myofibrils or other internal organelles like the nucleus. It also did not provide a prediction of where the myofibrils would be located within the cell. Several other models have followed suite, considering the interaction between focal adhesion dynamics and resulting traction stress measurements but not addressing myofibril

placement [55, 89, 88]. Consequently, previous models have been unable to recapitulate the internal architecture observed experimentally [67, 92].

In this work, we utilized the myofibril force-focal adhesion relation [8] to simulate the interplay between focal adhesion dynamics and cytoskeleton construction simultaneously, allowing to the development of a dynamically changing cytoskeletal network. Our model considered how a cell attached to a flat ECM island of a particular geometry might lead to alterations in the cytoskeleton, allowing us to explore the impact of cellular boundary cues on intracellular architecture. By controlling cell size and shape as well as nucleus size and location, we were able to generate myofibril networks that could vary depending on several stochastic factors. While these factors may influence the cell's cytoskeletal architecture, our approach provides useful information regarding the formation of any given cytoskeleton by linking myofibril maturation, the number of myofibril bundles present in the network and the ability to adapt to a changing focal adhesion distribution.

3.2 Results

3.2.1 Model overview

To explore the development and maturation of the myofibrils that comprise the cytoskeleton, our model consisted of two interacting components, which allowed for the visualization of myofibril curves within a simulated 2D cell geometry (Fig. 3.1). Focal adhesions were modeled using kinetic equations by considering the density of bound and unbound integrins, ρ_b and ρ^*, respectively (Eq. (3.1)-(3.2)). At each point in the cell containing some density of bound integrins, a net force $\mathbf{F}$ (Eq. (3.8)) was exerted, which accounted for adhesion reinforcement via integrin clustering and the influence of the forming or maturing cytoskeleton. Once a minimum density of bound integrins were present and contributing a force magnitude

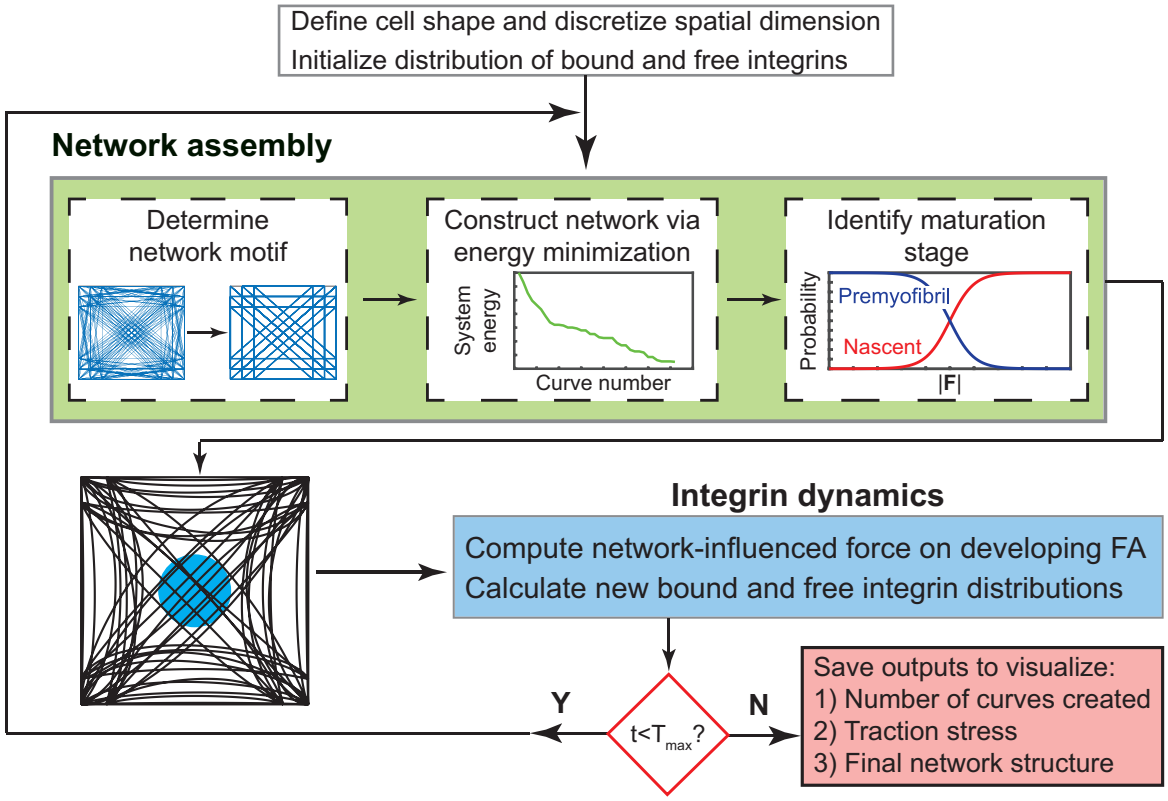

Figure 3.1. Schematic overview of major modeling components. Basic model implementation consists of an initialize stage where the cell geometry is predetermined and required parameters are set. The initial distributions of bound and free integrins are determined and the different model components are carried out as outlined in Materials and Methods.

sufficient enough to sustain a cytoskeletal connection, a premyofibril could be created.

To assemble the cytoskeletal network, the collection of viable anchoring points were identified and a template network was determined based on the net force vectors associated with each point. This template network defined the order in which the individual curves would be created. The probability of a constructed curve being at a particular stage of maturation was assumed dependent on the amount of force generated at the endpoints of the curve, with premyofibrils having smaller forces while larger forces indicated maturation into the nascent myofibril stage (Eq. (3.15)-(3.16)). The densities of free and bound integrins at each time step would respond to the cytoskeletal network that was constructed through a force-induced integrin recruitment term. In this way, developing focal adhesions would

be reinforced allowing for more myofibrils to be constructed. This would influence the net force exerted on the focal adhesions resulting in more integrins being recruited to the focal adhesion sites where the cycle would repeat.

Individual myofibrils were modeled as fourth order Bézier curves [20] with minimal bending energy. This was accomplished by identifying the starting and ending points for each curve according to the criteria described above. A net force vector **F** was associated with each point and used to determine the tangent vector to the curve at the designated point. The remaining control points defining the parametric curve were determined based on the endpoint tangent vectors and how to most effectively minimize the bending energy equation (Eq. (3.11)). To determine whether the constructed curve was viable, an energetic cost associated with placing a proposed curve within a developing network was included (Eq. (3.13)). By taking into account the energetic cost of constructing a myofibril coupled with the potential energetic cost of placing the constructed myofibril in the cell, only curves that contributed to the minimization of the system energy (Eq. (3.12)) were utilized to construct the cytoskeletal network.

3.2.2 Impact of the nucleus on the cytoskeleton

Since our model allows for the nucleus to influence the development of the cytoskeleton, we explored how the final network might be impacted by changes in the location and relative influence of the nucleus. The level of influence of the nucleus was associated with the energetic cost required to create a curve that crossed the nuclear boundary. A moderate level of influence corresponded to a relatively low energetic cost while a major level of influence corresponded to a higher energetic cost. For a baseline, the theoretical scenario where no nucleus was present in the square cell was simulated (Fig. 3.2A,B(i)). The nucleus was then placed in three different locations within the cell geometry and the resulting cytoskeletal

networks were evaluated. This was done in the cases where the nucleus was allowed a moderate level of influence on the cytoskeleton (Fig. 3.2A(ii)-(iv)) and when the nucleus was allowed a major level of influence on the cytoskeleton (Fig. 3.2B(ii)-(iv)). From the results of the simulations, it can be qualitatively observed that the presence of the nucleus impacts the behavior of the network near the nucleus location. When no nucleus was present, there was an increase in straight diagonal curves passing near the geometrical center of the cell. However, when the nucleus was taken into account, it became more energetically favorable to create curves that bended around the nucleus rather than go across it. As might be expected, the level of nuclear influence impacted the total energetic cost of creating the network. This could be seen qualitatively by the apparent decrease in the number of curves created for each nucleus location.

The change in cytoskeletal structure for each level of nuclear influence was quantified using the Co-Orientational Order Parameter (COOP) [34], where all cell pairs were considered (Fig. 3.2A,B(v)). This metric ranges from zero to unity and quantifies the level of consistency between pairs of structures. A COOP of one indicates the structures perfectly mimic each other while a value of zero means there is no consistency between the two structures. The metric can be calculated for different length scales, allowing for structural comparisons at a local level when a small length scale is designated while more global comparisons could be captured by using a large scale. Calculating the COOP at a large ($\sim$15 μm) length scale revealed high levels of global consistency regardless of nucleus placement. At a small ($\sim$1 μm) length scale, structural differences became more apparent. This could suggest that the mechanisms underlying the interaction between the cytoskeleton and the nucleus may be central to producing local variations in cytoskeletal networks experimentally. However, this may not hold true for elongated cells where there is less space for the myofibril bundles to occupy, resulting in more locally consistent structures. This could indicate that the level of influence of the nucleus might vary from cell to cell due to other intracellular factors.

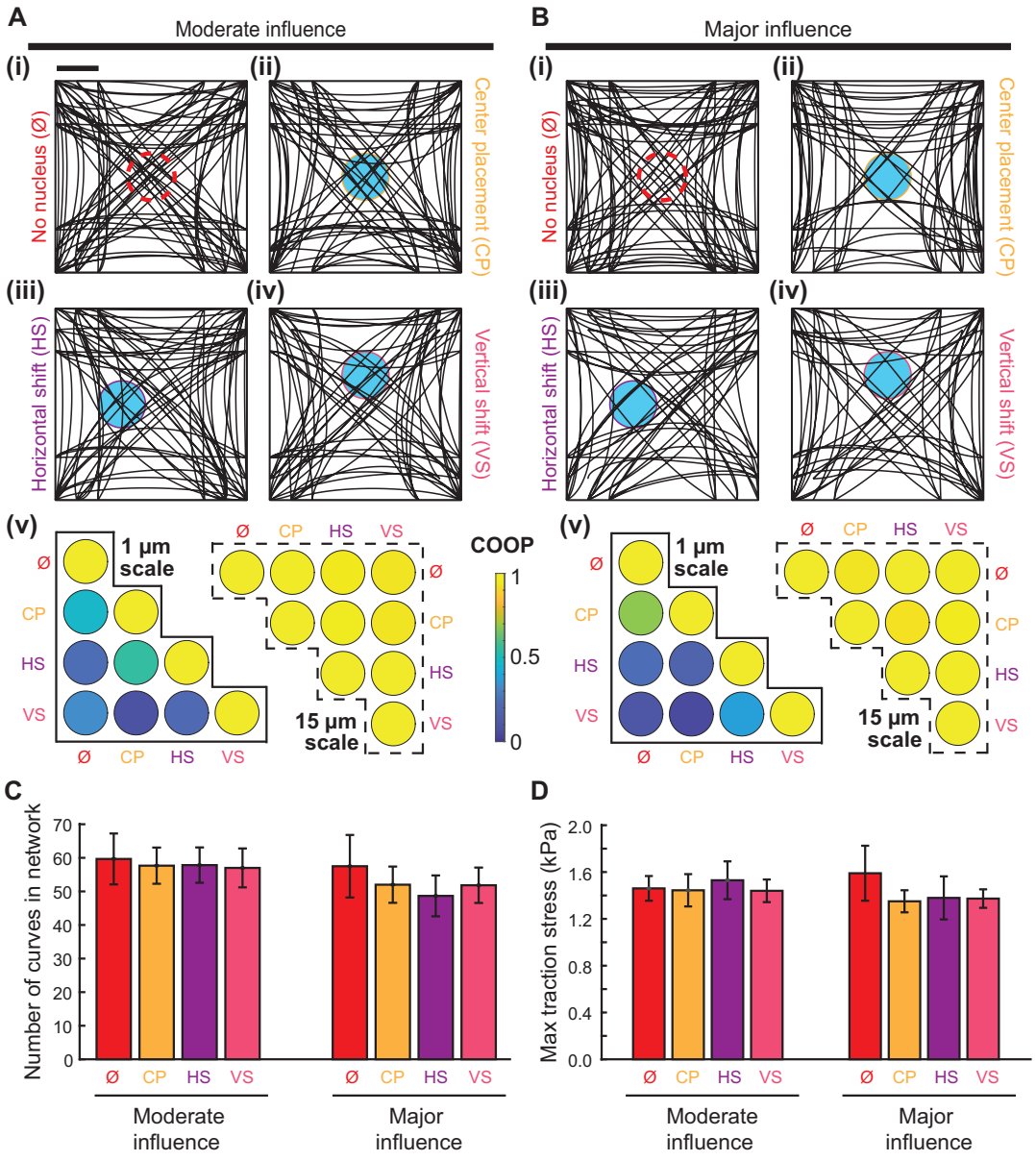

Figure 3.2. Influence of the nucleus on cytoskeletal properties. The nucleus was provided a level of influence on the cytoskeleton corresponding to the energetic cost of creating a curve that passes over the nucleus. This level of influence varies from moderate (A) to major (B). The location of the nucleus was altered to mimic the cases where there was no nucleus present (i), placed in the geometric center (ii), placed left of center (iii) or placed above the center point (iv). The COOP was applied at two different length scales to the networks obtained (v). After performing 6 simulations of each nucleus location in (A) and (B), the average number of curves created over all simulations was recorded (C) as well as the maximum traction stress (D), estimated using the magnitude of the net force at every point in the cell divided by unit cell area. Scale bar: 10 μm.

The impact associated with changing the amount of nuclear influence on the cytoskeleton was further quantified by performing multiple simulations where the nucleus location was changed. Due to the difference in resulting cytoskeletons for each scenario, the average number of curves created in each case was considered (Fig. 3.2C) as well as the average maximum traction stress generated (Fig. 3.2D). Consistent with qualitative observations, there was a general decrease in the average number of curves created when nucleus placement was fixed and level of influence was increased. Similarly for the average maximum traction stress, which consistently produced values within the typical range reported experimentally [67]. However, these differences were not statistically significant. Since there were no statistically significant differences in these cases and the nucleus is expected to play a larger role in elongated cells, a moderate level of nuclear influence was assumed for the remaining simulations. This allowed cytoskeletal networks to be created in rectangular geometries with variable aspect ratio.

3.2.3 Exploring force-length dependence

There has been evidence suggesting that the force exerted on developing focal adhesions may be tied to the cell geometry via a force-length relationship [8, 89]. Previous modeling has shown that in cells with geometries defined by several different lengths, a force-length relationship is likely to produce cytoskeletal networks more consistent with experimental findings compared to no force-length dependence [55]. However, identifying potential types of dependence requires the inclusion of length scales. Since our model is dimensionalized, it was used to explore two potential force-length relationships that may be applicable. The force equation consists of terms that scale with fiber length, designated $\tilde{f}$ (Eq. (3.17)). While this value is fixed for each geometry, the parameter α can be tuned to either 0 or 1, each representing a different type of force-length dependence. When $\alpha = 0$ (OFF), the force parameters maintain a consistent value for all shapes. This causes the force to be

dependent on an absolute-length value. When $\alpha = 1$ (ON), the force parameters are allowed to vary based on the maximum end-to-end fiber length within a cell geometry. Under this formulation, the force parameter values are scaled as a result of the changing cell geometry, which was classified as a relative-length dependence.

Multiple simulations were run on cell geometries with fixed area but different aspect ratios. In each simulation, the nucleus was randomly placed near the center of the geometry and allowed to have a moderate level of influence. For each aspect ratio, the number of curves and corresponding curve lengths were recorded along with the final maximum traction stress. There was a decrease in the average number of curves present in the final network for both force-length relationships explored (Fig. 3.3A). Increasing aspect ratio also resulted in longer curves being generated on average, with more consistent curve lengths observed in the relative length-dependence scenario (Fig. 3.3B). Overall, these results are consistent with what can be qualitatively observed in experimental cells [97, 80, 67]. However, there is a behavioral shift that occurs when considering the average maximum traction stress that is produced (Fig. 3.3C). Simulations utilizing the relative-length dependence produced traction stress values between ∼1-2 kPa, within the 1-3 kPa range reported for cells having these aspect ratios [67]. In contrast, simulations with the absolute-length dependence produced traction stress values that increased almost linearly with aspect ratio. This scenario almost universally produced traction stress values that were outside the physiological range. When coupled with the wide variability in curve lengths produced, a mechanism causing the force exerted on a focal adhesion to vary in this type of length-dependent manner seems unlikely. Therefore, for all other comparisons presented, a relative-length dependence ($\alpha = 1$) is assumed.

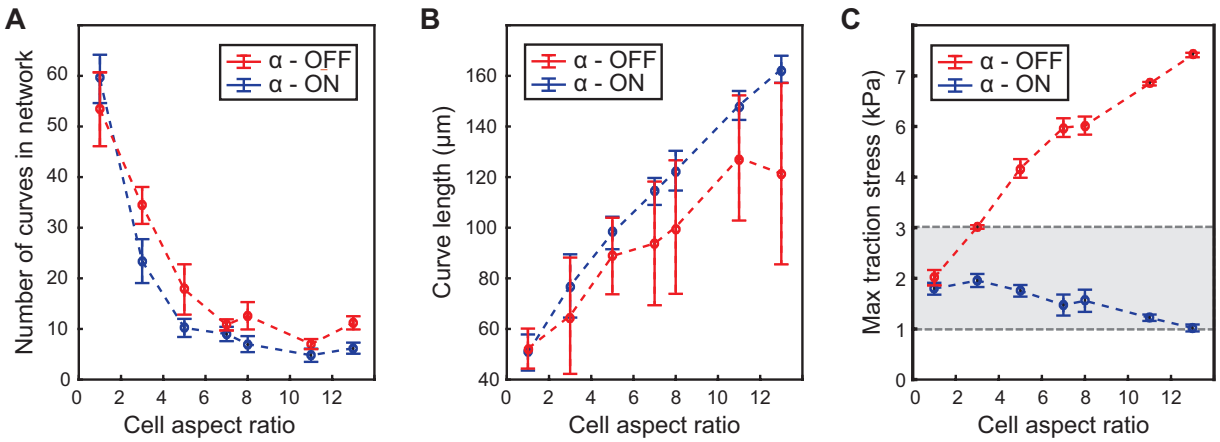

Figure 3.3. Testing length-dependence relationships. Model was implemented on rectangular geometries with aspect ratios varying from 1:1 to 13:1. For each aspect ratio, 6 simulations were performed and α was set to $\alpha = 0$ (OFF: absolute-length dependence) or $\alpha = 1$ (ON: relative-length dependence). The average number of curves created (A), the average curve length (B), and the average maximum traction stress (C) were computed for each aspect ratio. The shaded region identifies the range of average maximum traction stress values reported from the literature.

3.2.4 Structural consistency in experimental and simulated networks

Previous studies have reported that increasing cell aspect ratio results in an increase in intracellular alignment [97, 80]. The increase in alignment correlates with cytoskeletal networks having similar internal architecture and has been previously quantified using the COOP metric [36]. To test the viability of our model, this metric was applied to our model-generated networks for different cell geometry aspect ratios. In experimental cells, the COOP was seen to monotonically increase as the cell was elongated (Fig. 3.4A), demonstrating that aspect ratio influences the structural consistency of the cytoskeleton at both the small and large scales. When applied to model-generated networks, a similar trend was observed (Fig. 3.4B). At both length scales, the simulations demonstrate an increase in structural consistency as the cell geometry elongates.

Experimental cells were then grouped alongside the model-generated networks for each as-

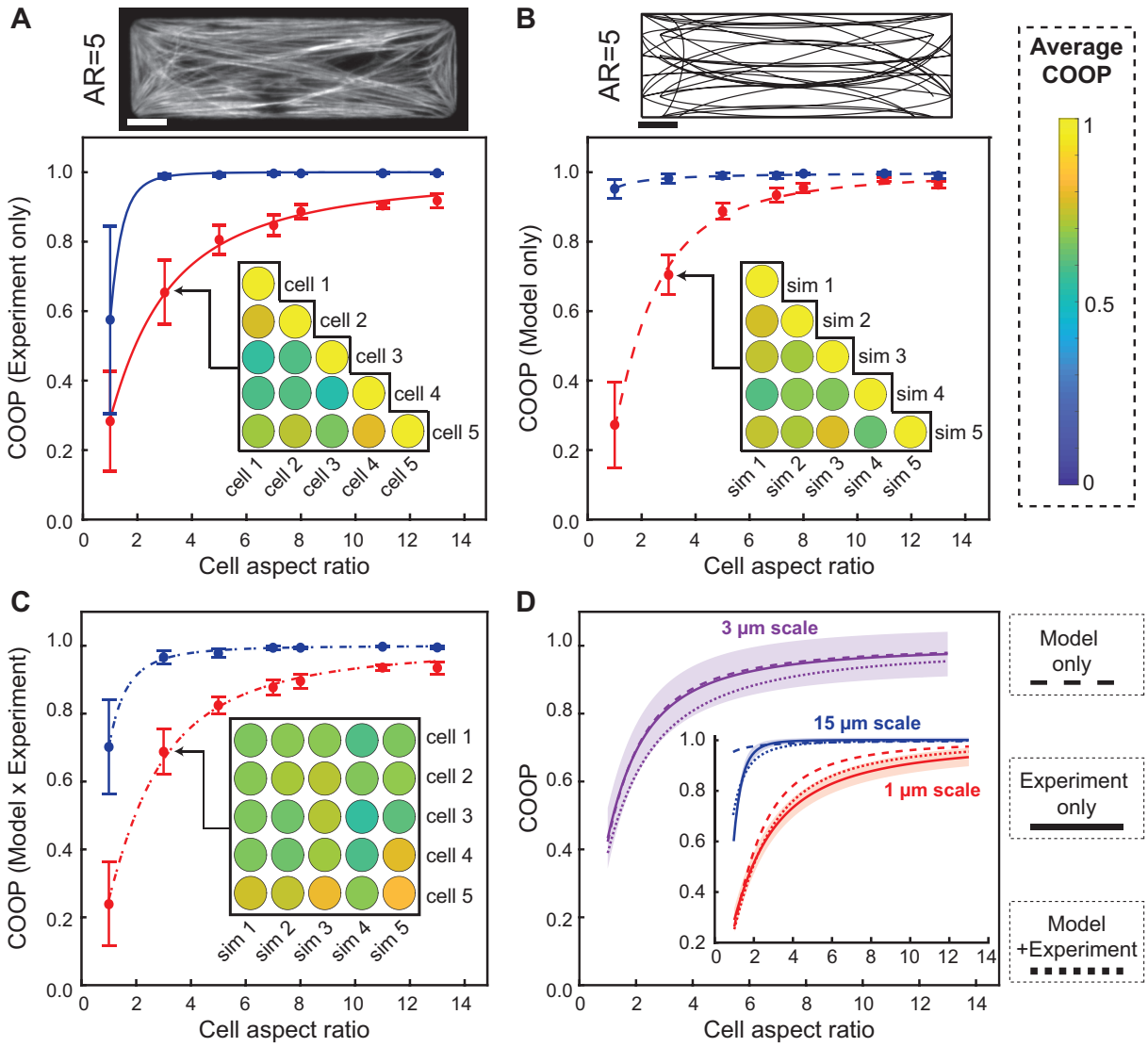

Figure 3.4. Testing structural consistency. The average COOP was computed at small (∼1 μm, red) and large (∼15 μm, blue) scales for experimental cells (A) and model-generated networks (B). At each aspect ratio, experimental cells and model simulated networks were combined into a single group and the average COOP was computed (C). The COOP was recorded within each aspect ratio by comparing all possible cell-cell pairs (A, B, C insets). For the 3 μm length scale, networks generated by the model simulations were combined with experimental cells into a single group and the corresponding COOP values (dotted lines) were computed (D). The group containing only experimental data (solid lines) and the group containing only model networks (dashed lines) were also computed for comparison. This was repeated at both the small and large length scales (D, inset). The shaded areas designate the 95% confidence region for the experiment only group. Scale bars: 10 μm.

pect ratio. Computing the COOP using the grouped data revealed a similar trend as the experimental data alone (Fig. 3.4C). This was further analyzed to determine whether the simulated networks could be distinguished from the experimental data. Accordingly, the group consisting of only experimental cells was used as a baseline. Previous results have demonstrated that in individual cells, the COOP varies depending on the length scale chosen with an inflection point around the 3-4 μm scale [36]. To test whether length scale might influence the viability of the model results, a 3 μm scale was included in the analysis. The fitted Hill functions for all data sets were plotted along with the 95% confidence band of the baseline group (Fig. 3.4D). When viewed together, the fitted functions for most data sets fell within the confidence region across the length scales analyzed. Notably, the grouped model/experiment data set fell within the confidence region for nearly all aspect ratios. These results demonstrate that the model-generated networks are structurally consistent with the experimental data for a variety of aspect ratios at different length scales.

3.3 Discussion

The cytoskeleton interacts and coordinates with numerous intracellular structures across several length scales [36, 131, 108]. As the cytoskeleton develops, the dense packing induces a physical competition for space between neighboring myofibril bundles. This also causes the cytoskeletal network to interact with other subcellular structures that occupy space within the cell such as the nucleus [48]. Until now, no technique had been developed that took into account spatial constraints to predict the exact placement of myofibril bundles within a cell. We addressed this by developing a theoretical model that used basic structural components to build a dynamically changing cytoskeletal network.

Our approach differs from previous attempts in several crucial aspects. Typically, cytoskeletal components are studied in isolation [40, 14, 86] and when multiple components are

combined, the emphasis is often placed on how contractility might influence the normalized traction stress magnitudes in different cellular regions [32, 144]. Our model links several structural components allowing for a direct exploration of network properties including the impact of nucleus location on a developing cytoskeleton (Fig. 3.2). Additionally, since most models take a non-dimensional approach [144, 55], the nature of the myofibril force-length dependence had not been fully explored. The force equation (Eq. (3.4)) was developed with parameters that incorporated length scales, making it possible to investigate whether dimension-dependent force-length relationships influenced cytoskeletal construction (Fig. 3.3A,B). Previous studies have demonstrated that cell contractility varies within 1-3 kPa [67, 89], which out model is able to capture using only the feedback between the distribution of focal adhesions and the developing cytoskeleton (Fig. 3.3C).

Within this range, however, the model is currently unable to recreate the precise dependence of traction stress on aspect ratio that has been observed in past experiments [67, 97]. This is likely due to the absence in the model of sarcomeric influence on cytoskeletal formation. Sarcomeres are the central contractile unit that make up the myofibrils [103, 108] and their alignment and registration correlate with cell aspect ratio in the same way that traction stress changes with cell aspect ratio [83, 31]. However, theoretical studies exploring force modulation via the sarcomeres have been difficult to produce because the alignment of sarcomeres depends on the location of the myofibril bundles. Future work in advancing this model will include incorporating sarcomeric registration into the developing network since it is now possible to visualize realistic cytoskeletal networks theoretically, allowing for the increasing-decreasing traction stress behavior to be captured.

In experimental cells subjected to the same environmental conditions, the overall cytoskeletal structure is largely consistent yet each cell exhibits variations in internal architecture [92]. While this phenomenon has been studied in individual cells using multi-scale quantitative analysis [36], previous modeling attempts have been unable to reproduce networks that are

structurally similar to experimental cells while also capturing cell-to-cell variability. Our approach produced individual myofibril bundles within the cell geometry, allowing for direct structural comparisons between model-generated networks and experiments. In all cases, a diverse array of meshworks were produced, due to the stochasticity built into the model equations, but the process of minimizing the cost associated with the developing mesh resulted in recurring structural properties. In addition to being qualitatively similar to experimental cells, the simulations quantitatively recreated the multi-scale relationship between structural consistency and cell aspect ratio (Fig. 3.4A,B). When the model-generated networks were compared with the experimental cells, the results were consistently within the 95% confidence region produced by comparing experimental cells to each other (Fig. 3.4C,D). Whereas previous models consistently yielded the same steady state outcomes [144, 55], our approach produced unique network with each simulation, as is seen in the experimental cells.

3.4 Conclusion

The modeling framework outlined in this work provides a platform for future studies concerning the development of the cytoskeletal network and how it may be connected to cell contractility. A key achievement of our approach is the ability to recreate networks that demonstrate cell-to-cell variability using only basic cellular components. By modeling the feedback between focal adhesion maturation and cytoskeletal formation, it is possible to establish the exact placement of myofibril bundles for a specific cell. The ability to create and visualize individual myofibril curves within a two-dimensional geometry is an essential first step towards elucidating the influence of intracellular structures such as the nucleus on cellular organization and contractility. Since only a few processes were emphasized, there is potential for future model development by incorporating additional cellular components into the modeling framework. For instance, now that the location of a myofibril bundle can

be determined, the sarcomeres that make up the bundle can be modeled and the influence of their registration can be analyzed. Thus, the model may be extended and used to explore how subcellular components like sarcomeres regulate cellular phenomena such as contractility. Our approach demonstrates that the cytoskeleton may form based on the unique subcellular interactions occurring within the specific cell. These interactions give rise to physical constraints that dictate which connections need to be established in order to create the most energetically beneficial and efficient cytoskeletal network.

3.5 Materials and Methods

3.5.1 Model formulation

Integrin based focal adhesion model

The model is based on a simplified classification of integrins proteins into either a bound or unbound state, denoted ρ_b and ρ^*, respectively. Unbound integrins have a spontaneous binding rate k_0 and a force-induced binding rate that increases linearly with force, $k_1|F|$. A bound integrin becomes unbound due to the force exerted on it by the myofibril and this unbinding rate is assumed to be of the form $k_{-1}\exp\big(|\mathbf{F}|/F_0\big)\rho_b$. This gives the kinetic equation for the density of bound integrins:

$$\frac{\partial \rho_b}{\partial t} = (k_0 + k_1|\mathbf{F}|)\rho^* - k_{-1}e^{|\mathbf{F}|/F_0}\rho_b. \tag{3.1}$$

The density of free integrins is derived by assuming that unbound integrins can diffuse throughout the 2D cell at a much faster rate than all other processes in the cell, resulting in

$$\rho^* = \frac{1}{|\Psi|}\int_{\Psi}(\overline{\rho} - \rho_b)d^2\mathbf{x}', \tag{3.2}$$

where $\overline{\rho}$ is the average integrin density in the cell defined by the geometry Ψ.

Once integrins are converted from a free to bounded state, they anchor to the cell membrane and produce an adhesion force,

$$F_{adh}(\mathbf{x}) = k_{CS}\, dA_{FA,p}\frac{\rho_b}{\rho_b + \rho_0}\hat{e}. \tag{3.3}$$

Here, k_{CS} denotes the equilibrium adhesion force and $dA_{FA,p}$ is the minimum focal adhesion area required for a premyofibril to form. Any integrin within the cell island may connect to any other integrin so long as both connectors have a sufficient adhesion force. The description for the cytoskeletal force prior to the formation of myofibrils may be developed based on the fraction of integrins contributing to force production at any appropriate point:

$$\mathbf{F}_{\rho}(\mathbf{x}, t) = \tilde{f}_{\rho}R(\mathbf{x})H(R(\mathbf{x}) - R_t)\int_{\Psi}R(\mathbf{x}')H(R(\mathbf{x}') - R_t)[\mathbf{x}' - \mathbf{x}]d^2\mathbf{x}', \tag{3.4}$$

where $H(\cdot)$ is the heaviside function, R_t represents the fraction of bound integrins that must contribute to force in order to support a cytoskeletal connection, and $R(\mathbf{x})$ is the fraction of bound integrins that contribute to force production modeled using a Langmuir Isotherm,

$$R(\mathbf{x}) = \frac{\rho_b(\mathbf{x}, t)}{\rho_b(\mathbf{x}, t) + \rho_0}. \tag{3.5}$$

Once the cytoskeletal force is sufficiently strong, a premyofibril may be built with its own force contribution $\mathbf{F}_p$. Fiber maturation is determined by the amount of force generated so that a premyofibril may be reclassified as a nascent myofibril with force term $\mathbf{F}_n$ once a

sufficient amount of force is generated:

$$\mathbf{F}_p(\mathbf{x},t) = \tilde{f}_p \int_{\Psi_{FA}} \Pi_p(\mathbf{x},\mathbf{x}') \frac{N_F(\mathbf{x},\mathbf{x}')}{N_{tot}} L_{tot}(\mathbf{x},\mathbf{x}') \hat{v}(\mathbf{x},\mathbf{x}') d^2\mathbf{x}' \tag{3.6}$$

$$\mathbf{F}_n(\mathbf{x},t) = \tilde{f}_n \int_{\Psi_{FA}} \Pi_n(\mathbf{x},\mathbf{x}') \frac{N_F(\mathbf{x},\mathbf{x}')}{N_{tot}} L_{tot}(\mathbf{x},\mathbf{x}') \hat{v}(\mathbf{x},\mathbf{x}') d^2\mathbf{x}', \tag{3.7}$$

where $N_F(\mathbf{x},\mathbf{x}')$ denotes the number of fibers connecting $\mathbf{x}'$ and $\mathbf{x}$, N_F/N_{tot} identifies the fractional contribution of the connectors, Π_i denotes the probability that at least one fiber is of type i, and L_{tot} is the total length of the connections spanning $\mathbf{x}'$ and $\mathbf{x}$. The net force associated with the focal adhesion at $\mathbf{x}$ is described by

$$\mathbf{F}(\mathbf{x},t) = \mathbf{F}_{adh}(\mathbf{x},t) + \mathbf{F}_\rho(\mathbf{x},t) + \mathbf{F}_p(\mathbf{x},t) + \mathbf{F}_n(\mathbf{x},t). \tag{3.8}$$

Optimization driven myofibril model

Cytoskeletal network construction was performed at each time point in a discrete fashion utilizing a finite collection of points within the cell geometry for which $\mathbf{F}(\mathbf{x}) \geq \mathbf{F}_{thresh}$. The points were then sorted into distinct pairs and ranked to create a potential collection of myofibrils having the assigned endpoints. Each myofibril was constructed as a fourth-order parametric Bézier curve whose bending energy could be described by

$$E_B = \frac{EI}{2} \int_0^{L_c} |\gamma''(t)|^2 dt = \frac{l_p k_B T}{2L_c^3} \int_0^1 |r''(s)| ds,$$

where $r(s)$ refers to the standard Bézier curve representation, L_c is the length of the curve, l_p denotes the persistence length of the curve, k_B is the Boltzmann constant and T is the absolute temperature in Kelvin [128, 37]. The standard curve r can be described by desig-

nating control points $P_0, \ldots, P_4$ where P_0 and P_4 denote the starting and ending points for the curve. Writing the tangent vectors at P_0 and P_4 as v_1 and v_2, respectively, the control points P_1 and P_3 satisfy

$$P_1 = P_0 + \frac{|P_4 - P_0|}{\alpha_{P_1}|v_1|} v_1 \tag{3.9}$$

$$P_3 = P_4 + \frac{|P_4 - P_0|}{\alpha_{P_3}|v_2|} v_2 \tag{3.10}$$

where α_{P_1} and α_{P_3} are stochastic constants which help define the control polygon through which each curve can be constructed. For our purposes, requiring $\alpha_{P_1}, \alpha_{P_3} \geq 4$ yielded curves with bending motifs that we similar to those seen in experimental images. Using the control points, the bending energy equation was rewritten as

$$E_B = \frac{EI}{L_c^3} \left(72 \left[\frac{5}{6}|Q_0|^2 + \frac{2}{3}|Q_1|^2 + \frac{1}{6}|Q_2|^2 \right] \right), \tag{3.11}$$

where

$$\begin{aligned} Q_0 &= \tfrac{1}{\sqrt{30}} \left(-\sqrt{3}P_0 + 2\sqrt{3}P_1 - 2\sqrt{3}P_3 + \sqrt{3}P_4 \right) \\ Q_1 &= \tfrac{1}{\sqrt{30}} \left(2P_0 - 3P_1 + 2P_2 - 3P_3 + 2P_4 \right) \\ Q_2 &= \tfrac{1}{\sqrt{30}} \left(\sqrt{5}P_0 - 2\sqrt{5}P_2 + \sqrt{5}P_4 \right). \end{aligned}$$

This function was minimized by determining the control point P_2 that optimized equation (3.11), depending on whether the constructed curve intersected the nucleus.

To build the myofibril network, the energetic cost of constructing a myofibril and the energetic cost of placing the constructed myofibril in the cell were utilized to determine the total energy

within the network:

$$E^*_{sys} = \sum_{f_k} [(E^*_B(f_k) - E^{\max}_B(f_k)) + E^*_{def}(f_k)]. \tag{3.12}$$

where f_k denotes the kth myofibril constructed. A constructed curve was accepted into the network if it's inclusion contributed to reducing the total energy of the system. The first summation term in (3.12) describes the energetic cost of constructing a myofibril and utilizes the normalized form of the simplified bending energy equation (3.11), $E^*_B = E_B/(k_B T)$. The second summation term represents the total energetic change in the membrane, normalized to the initial membrane area, due to the placement of myofibril f_k:

$$E^*_{def}(f_k) = \frac{1}{A} \int_\Psi \left[E^*_{\text{mem}}(\mathbf{x}|f_k \text{ is placed}) - E^*_{\text{mem}}(\mathbf{x}|f_k \text{ is not placed}) \right]. \tag{3.13}$$

This deformation equation considers the total change in energy induced by the placement of a myofibril within the network which is influenced by the cumulative height h of stacked fibers within dA:

$$E^*_{mem}(\mathbf{x}|f_k) = \frac{\kappa_b}{2} \left(\nabla^2 h(\mathbf{x}|f_k) \right)^2 + \frac{\tau}{2} \left(\nabla h(\mathbf{x}|f_k) \right)^2. \tag{3.14}$$

Once the cytoskeletal network was determined, each constructed fiber was classified as either a premyofibril or nascent myofibril. The maturation process is assumed to be force-induced since there are suggested correlations between myofibril type, focal adhesion size, and the force generated by a myofibril [8, 120]. We required both endpoints generate a sufficient force $\mathbf{F}^*$ in order to be created and both endpoints must pass a secondary force threshold $\mathbf{F}_c$ in order for maturation to begin. To this end, we set $\mathbf{F}_{\min} = \min(|\mathbf{F}(\mathbf{x})|, |\mathbf{F}(\mathbf{x}')|)$ and modeled maturation as a second-order phase transition [115] where the energetic cost of maintaining

the constructed curve in the premyofibril or nascent myofibril stage was described as

$$E_p^* = \begin{cases} E_B^* & \mathbf{F}_{\min} \geq \mathbf{F}^* \\ 0 & \mathbf{F}_{\min} < \mathbf{F}^* \end{cases}$$

$$E_n^* = \begin{cases} E_0^* - \frac{(a^*)^2}{4b^*}\left(\frac{1}{\mathbf{F}_{\min}-\mathbf{F}^*} - \frac{1}{\mathbf{F}_c}\right)^2 & \mathbf{F}_{\min} \geq \mathbf{F}_c \\ E_0^* & \mathbf{F}^* \leq \mathbf{F}_{\min} \leq \mathbf{F}_c \\ 0 & \mathbf{F}_{\min} < \mathbf{F}^* \end{cases}$$

where E_0^*, a^* and b^* are tunable parameters designed to make it more energetically beneficial to start as a premyofibril and mature to a nascent myofibril once the fiber can maintain a desired amount of force. The maturation energies were then used to determine the probability that a curve is in a given state of maturation:

$$\Pi_p = \frac{1}{1+e^{-\Delta E^*}} \tag{3.15}$$

$$\Pi_n = \frac{1}{1+e^{\Delta E^*}} \tag{3.16}$$

where $\Delta E^* = E_m^* - E_p^*$.

Incorporating fiber-length dependence

Since there are three force constants within the force equation (Eq. (3.8)), we expect them to all have the same units since each integral term is meant to have a similar meaning. This means that $\tilde{f}$ has units Pa/m which we interpret as the stress exerted on developing/maturing focal adhesion relative to an effective length. Previous studies have shown that there is a constant stress exerted on focal adhesions of $T_{est} = 5.5 \pm 2nN/\mu m^2$ [8]. This

stress propagates along segments of the cytoskeleton but how effective the force is translated from one cytoskeletal length segment to the next may depend on many different factors. Previous models have demonstrated that the organization of the myofibril network may be more qualitatively similar to experimental results when the force term is fiber-length dependent [55]. We incorporate this length-dependent behavior into our $\tilde{f}$ parameter by writing

$$\tilde{f} = \frac{\{\text{Stress exerted on a FA}\}}{\{\text{Effective myofibril length}\}},$$

where the effective myofibril length may be determined by the geometry of the cell. Specifically, we assume this length term, if applicable, is the maximum length of a straight myofibril within the prescribed cell geometry, $L_{\max}$. With this inclusion, the force term may vary based on the type of length dependence:

$$\tilde{f} \propto \frac{T_{est}}{L_{\max}^{\alpha}} \tag{3.17}$$

where $\alpha = 0$ would create an absolute-length dependence where $\tilde{f}$ is constant regardless of cell geometry and $\alpha = 1$ would create a relative-length dependence where $\tilde{f}$ varies. All model implementation and analysis codes have been made available on Github: `https://github.com/Cardiovascular-Modeling-Laboratory/singlecell`.

3.5.2 Ethics statement

All animals were treated in agreement with the guidelines of the Institutional Animal Care and Use Committee of UCI guidelines (IACUC Protocol No. 2013-3093). NIH Guide for the Care and Use of Laboratory Animals recommendations were followed and procedures were in accordance with existing federal (9 CFR Parts 1, 2, & 3), state, and city laws and regulations governing the use of animals in research and teaching. CO2 inhalation followed by cervical dislocation at a ULAR facility was used to euthanize the adult Sprague-Dawley rat. To

minimize the stress the dams experience when their pups are taken, dam's euthanasia was done before pup sacrifice. In accordance with humane standards, the pups were subsequently taken to the core lab where each neonatal rat pup was euthanized by decapitation. As stated in the "AVMA Guidelines for the Euthanasia of Animals: 2013 Edition" (published by the American Veterinary Medical Association), this euthanasia method adheres to the most current standards and maintains scientific validity of the cell cultures.

3.5.3 Fibronectin patterning

Large, rectangular cover glass (Brain Research Laboratories, Newton, MA) was sonicated, then spin coated with 10:1 Polydimethylsiloxane (PDMS; Ellsworth Adhesives, Germantown, WI). The coated glass was placed in a 60^oC oven to cure overnight and then cut into, approximately, 13 mm$\times$15 mm rectangular coverslips to fit in a 12-well plate. Fibronectin (FN; Fischer Scientific Company, Hanover Park, IL) was patterned onto the coverslips to have islands of a variety of shapes with areas of 1250 μm^2 or 2500 μm^2 using microcontact printing, as previously described [34, 36]. The FN-patterned coverslips were placed in a solution of 5 g Pluronics F-127 dissolved in 0.5 L sterile water for 5 min and rinsed three times with room temperature phosphate-buffered saline 97 (PBS; Life Technologies, Carlsbad, CA) in order to block the cells from attaching outside of FN lines.

3.5.4 Neonatal rat ventricular myocyte (NRVM) cell culture

As previously described [64, 36, 34], neonatal rat ventricular myocardium was extracted from two-day old Sprague Dawley rats (Charles River Laboratories, Wilmington, MA). The cardiomyocytes were then isolated from the ventricular myocardium as previously described [64, 36, 34]. Cells were counted and seeded onto FN coated coverslips at a density of 1M cells per well in a 6-well plate and 400K per well in a 12-well plate. After 24 hours, dead cells

were washed away with PBS and remaining cells are fed with 10% FBS M199 culture media. Another 24 hours later, the 10% M199 was replaced with warm 2% FBS M199 culture media.

3.5.5 Fixing, immunostaining and imaging

Cells were fixed with warm 4% paraformaldehyde (Fisher Scientific, Hanover Park, IL) supplemented with 0.001% Triton X-100 (Sigma-Aldrich, Inc., St. Louis, MO) in PBS for 10 minutes, as previously described [64, 36, 34]. Cultures were then immunostained for actin (Alex Fluor 488 Phalloidin; Life Technologies, Carlsbad, CA), sarcomeric α-actinin (Monoclonal Anti-α-actinin; Sigma Aldrich, Inc., St. Louis, MO), nuclei (4',6'-diaminodino-2-phenlyinodol (DAPI; Life Technologies, Carlsbad, CA), and FN (polyclonal rabbit anti-human fibronectin; Sigma Aldrich, Inc., St. Louis, MO), as previously described [64, 36, 34]. Secondary staining was applied using tetramethylrhodamine-conjugated goat anti-mouse IgG antibodies (Alexa Fluor 633 Goat anti-mouse or Alexa Fluor 750 Goat anti-mouse; Life Technologies, Carlsbad, CA) and goat anti-rabbit IgG antibodies (Alexa Fluor 750 goat anti-rabbit or Alexa Fluor 633 Goat anti-rabbit; Life Technologies, Carlsbad, CA). The images were collected using an IX-83 inverted motorized microscope (Olympus America, Center Valley, PA) with an UPLFLN 40x oil immersion objective (Olympus America, Center Valley, PA) and a digital CCD camera ORCA-R2 C10600-10B (Hamamatsu Photonics, Shizuoka Prefecture, Japan). Raw images as well as all other relevant data have been deposited in the Dryad repository: `https://doi.org/10.7280/D1CT1C`.

3.5.6 Image analysis

Image analysis of experimental data and model simulations was performed using previously created custom MATLAB codes [34, 36]. Structural comparisons were made by computing the co-orientational order parameter (COOP) for each cell pair. Images were segmented into

grids and the length of each grid square could vary from 1 μm to approximately 50 μm. The COOP ranges from 0 to 1 and is determined by computing the maximum eigenvalue of the structural tensor, as previously described [34].

3.5.7 Statistical analysis

Results are expressed using the mean with error bars representing the standard deviation. One-way analysis of variance (ANOVA) with the Tukey-Kramer test for pairwise comparisons was used to determine statistical significance. A p-value less than 0.05 was considered statistically significant.

Chapter 4

Exploring the impact of cytoskeletal organization on nuclear eccentricity

4.1 Introduction

In Chapter 3 we modeled the developing cytoskeletal network by allowing the nucleus to influence myofibril bundle placement. Under this formulation, the interaction between the cytoskeleton and the nucleus was dependent on the location and shape of the nucleus, which were assumed fixed at every time point. However, there is growing evidence linking cytoskeletal arrangement to changes in nuclear morphology [68, 131]. While this is particularly true in spreading cells, several studies have used micropatterned fibronectin islands to link cell geometry with nuclear shape. In particular, it has been demonstrated that there is a correlation between nuclear eccentricity and cell aspect ratio with elongated cells containing elongated nuclei [129, 131]. This is hypothesized to be caused by the interactions between the cytoskeleton and the nucleus.

Several studies have proposed linking cell aspect ratio to nuclear deformations by viewing the

nucleus as an elastic sphere surrounded symmetrically by parallel myofibrils which exhibit a compressive load on the sphere [129, 131]. By assuming these myofibrils are anchored at the cell periphery, the cell geometry can influence the compressive load and thereby be linked to the amount of nuclear deformation. This framework is often utilized to estimate physical properties of the nucleus since the final nuclear shape is known and the amount of compressive force may be estimated using data obtained from experimental techniques [121, 131]. However, if the physical properties of the nucleus are known, then our model outputs may be used to estimate the compressive load exerted on the nucleus via the cytoskeleton and determine the resulting change in nuclear shape. With this in mind, in this chapter we present a preliminary model designed to test whether we could effectively link these two cellular constructs using results from Chapter 3.

4.2 Model

4.2.1 Estimating nuclear eccentricity via spherical compression equations

We considered a cell at steady state consisting of an initially spherical nucleus surrounded by stress fibers which interact with the nucleus. These interactions result in the nucleus deforming due to the cytoskeleton exerting a compressive force. Assuming a constant 2D area, the initial 2D shape of nucleus was described using a circle with radius R and the final deformed shape was modeled as the ellipse $(x/a_e)^2 + (y/b_e)^2 = 1$ where a_e and b_e defined the major and minor axes of the ellipse, respectively. Since the final nuclear height d satisfied $d = 2b_e$, the amount of nuclear deformation α was computed as the difference between the initial and final nuclear height, $\alpha = 2R - d$. Once the amount of nuclear deformation was determined, the major and minor axes for the final deformed nucleus were calculated using

$b_e = R - \alpha/2$ and $a_e = R^2/b_e$. Assuming $a_e > b_e$, the eccentricity of the resulting ellipse was computed using

$$\epsilon = \sqrt{1 - \left(\frac{b_e}{a_e}\right)^2}. \tag{4.1}$$

To obtain the amount of deformation, the nucleus was modeled using the equations for an elastically deforming sphere compressed between two parallel plates. For our preliminary analysis, the load magnitude was determined using the force outputs at the final time point of our cytoskeleton model. Given an initial nuclear radius R and compressive load F, the Tatara et. al model [121] estimates the total amount of spherical deformation α as

$$\alpha = \frac{3(1-v_N)^2}{2E_N a}F - \frac{2Ff(a)}{\pi E_N} \tag{4.2}$$

where

$$a = \left(\frac{3(1-v_N)^2 RF}{4E_N}\right)^{1/3} \tag{4.3}$$

$$f(a) = \frac{2(1+v_N)R^2}{(a^2+4R^2)^{3/2}} + \frac{1-v_N^2}{(a^2+4R^2)^{1/2}}. \tag{4.4}$$

In this formulation, v_N denotes the Poisson's ratio of the sphere, E_N denotes the Young's modulus of the sphere, and a describes the contact radius between the compressive plate and the sphere.

4.2.2 Estimating nuclear compression load

To determine the amount of nuclear deformation resulting from interactions with the cytoskeletal network, we employed (4.2)-(4.4) where the compressive load F was obtained using the outputs at the final time point of the cytoskeleton model presented in Chapter 3. Specifically, we utilized our model's predicted net focal adhesion developmental force $\mathbf{F}$ to determine the normal forces acting on the nucleus. The load exerted by the parallel plates was viewed as a pair of pseudo-curves anchored on either side of the nucleus, designated F_{c_1} and F_{c_2} (see Fig. 4.1). To develop the normal force associated with a curve, F_c, two anchoring points $\mathbf{x}_1$ and $\mathbf{x}_2$ where chosen on the cell boundary to the left and right of the nucleus, each of which had an associated force vector $\mathbf{F}(\mathbf{x}_1)$ and $\mathbf{F}(\mathbf{x}_2)$. The curve c formed angles θ_1 and θ_2 with the horizontal as dictated by the associated force vector, $\tan\theta_k = \mathbf{F}_y(\mathbf{x}_k)/\mathbf{F}_x(\mathbf{x}_k)$. Additionally, since our net force $\mathbf{F}(\mathbf{x}_i)$ accounted for all myofibrils connected to $\mathbf{x}_i$, we made the simplifying assumption that the magnitude of this force is distributed across all available connections according to the average number of expected connections at any given point, N, defined as the ratio of the total number of connections in the network to the total number of anchorage points. The expected compressive load by curve c on the nucleus was taken to be the average of the normal forces obtained from each endpoint,

$$F_c = \frac{1}{2}\left[\frac{\mathbf{F}_x(\mathbf{x}_1)}{N}\tan\theta_1 + \frac{\mathbf{F}_x(\mathbf{x}_2)}{N}\tan\theta_2\right]. \tag{4.5}$$

The total nuclear compressive load F_{tot} was defined as $F_{tot} = |F_{c_1} - F_{c_2}|$, where the minus sign accounts for the difference in direction of the normal forces generated by curves c_1 and c_2. Due to the built-in variation associated with our cytoskeletal model, the force data outputted could vary depending on the network that was developed. To account for the influence of this variation, 6 simulations of our cytoskeletal model were implemented. Each simulation predicted its own unique compressive load value and the average total compressive load

across all simulations, $\langle F_{tot} \rangle$, was computed. The final nucleus shape was then determined by setting $F = \langle F_{tot} \rangle$ in equations (4.2)-(4.4) and computing the resulting eccentricity using (4.1).

4.3 Results

Individual square and rectangular cardiomyocytes having approximate aspect ratios 3:1, 5:1, 7:1 and 9:1 with fixed areas of 1250 μm^2 were used to demonstrate our ability to recreate nuclear compression data (Fig. 4.1A-F). The Young's modulus and Poisson's ratio for the nucleus have been estimated in the literature to be in the range of 1-10 kPa and 0.1-0.5, respectively [16, 48, 68]. After fixing these parameters, we used our cytoskeleton model presented in Chapter 3 to generate 6 potential myofibril networks per aspect ratio. For each of these simulations, the total compressive load being exerted on an elastically deforming nucleus was estimated by computing equation (4.5) for two curves with specified endpoints, representing the cumulative influence of the network on the nucleus. The average total compressive load $\bar{F}_{tot}$ across all simulations was then computed and utilized in equations (4.2)-(4.4) to determine the corresponding eccentricity of the deformed nucleus.

4.3.1 Recapitulating changes in nuclear eccentricity

Previous studies have demonstrated that there is a nonlinear relationship between the aspect ratio of a spread cell and the amount of nuclear elongation [129]. Utilizing the Tatara et al. spherical compression model in conjunction with our cytoskeletal model, we are able to mimic this general trend (Fig. 4.1I). Not only does our model capture how the nucleus tends to become narrower as the cell becomes narrower, our model produced eccentricity values that were generally consistent with those obtained from the experimental data. The exception

is the predicted nuclear eccentricity for the moderate (7:1) aspect ratio, which is slightly below the experimentally observed values. This result might be expected given the nature of the traction stress values predicted by our cytoskeletal model. Namely, our cytoskeletal model is currently unable to recreate the increase in traction stress that is observed at the 7:1 aspect ratio, resulting in lower force values in our simulated cell. As these force value directly influence the compressive load exerted on the nucleus, it may be reasonable for our formulation to output a lower compressive load, hence a lower eccentricity, at this aspect ratio.

4.3.2 Potential ability to study changes in nucleus location

Preliminary explorations regarding the location of the nucleus demonstrated that the nucleus does not always settle in the geometrical center of the cell. Rather, it often appears to be slightly off center (see Fig. 4.1B,D) with more variability observed in the square cell compared to the rectangular cells. Since our cytoskeleton model allows us to generate and visualize cytoskeletal networks, we may use our model outputs to not only explore nuclear morphology but also how the cytoskeletal network may cause changes in the location of the nucleus. As an initial exploration into this possibility, we used our simulated networks to determine the change in the density of the network on either side of the nucleus. In particular, we identified symmetric points on the top and bottom of the nucleus and recorded the number of curves from the network that fell within a small region of each point. The density of the network near the point of interest was then computed as the ratio of the number of curves within the region to the total number of curves within the network. The average difference in the network density on either side of the nucleus is summarized in Fig. 4.1I. A positive value corresponds to more fibers near the top of the nucleus compared to the bottom while a negative value suggests the opposite. The nonzero values seen in Fig. 4.1I may suggest that the network is not symmetric around the nucleus and so if either side has a designated

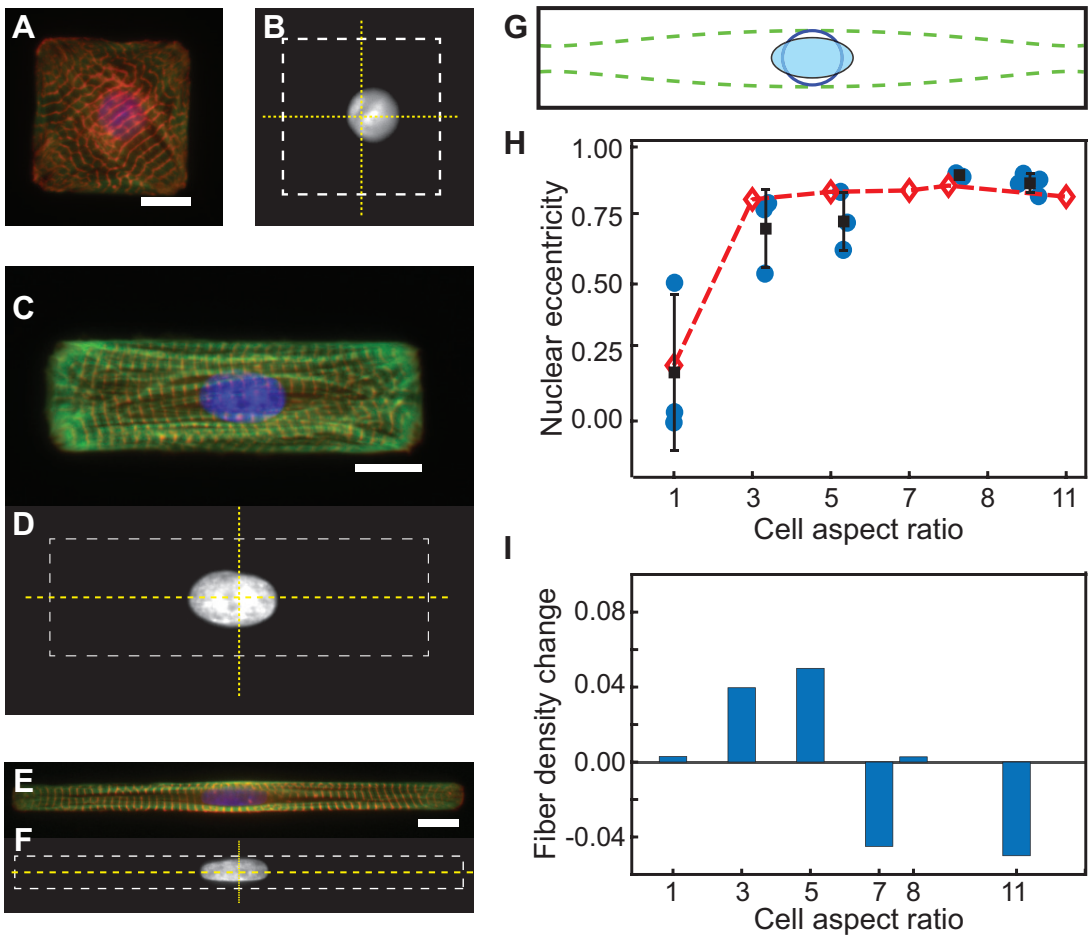

Figure 4.1. Model predicts how nuclear eccentricity will vary with cell aspect ratio. *First column:* A sample of the 1250 μm^2 experimental cells used including a square (A), 3:1 rectangle (C) and 10:1 rectangle (E). The nuclei were isolated for each cell (B, D, and F) to determine experimental nuclear eccentricity (mean $\pm$ SD). *Second column:* A schematic representation of the nuclear compression model (G) was used to the compressive load exerted on the deformable nucleus. (H) Model predicted compressive loads allowed for an estimation of the amount of nuclear deformation. The predicted nuclear eccentricity ($-\diamond-$) was compared to the eccentricity data (■), showing a similar trend. (I) The density of the simulated cytoskeleton network on either side of the nucleus can be estimated to determine whether the nucleus would be expected to move from its original location. Scale bars: 10 μm.

number of network curves exerting a force on the nucleus, one might expect the nucleus to move in accordance with the change in network density. This may be applicable to exploring whether or not the cytoskeleton plays a role in the final location of the nucleus.

4.4 Conclusions

We have demonstrated that it is possible to use a spherical deformation model [121] in conjunction with our cytoskeletal model to explore how the cytoskeleton may influence nuclear morphology. In the future, our cytoskeletal model may even be able to provide insight into why the final location of the nucleus seems to vary in experimental data. As a first step towards further linking two distinct cellular structure, our initial results are promising though more development is needed.

Chapter 5

Summary and future directions

The models developed have recreated and elucidated information concerning several intracellular properties across various spatial scales. Notably, we have allowed for the interplay of several cellular components that had previously been studied in isolation [121, 89, 40]. This provides several potential areas to pursue for future work which can be broadly grouped into two categories. Firstly, the interplay that has been explored thus far can be further extended by providing additional coupling between the various components. Alternatively, the current modeling approaches can be refined by addressing some of the simplifications that were made initially. Both categories provide a platform to expand on the working components of each model while also addressing some of the current limitations.

The model proposed in Chapter 2 allowed for the exploration of early stage premyofibril formation. By focusing on the distribution of α-actinin, we reproduced the clustering behavior and eventual pattern formation found in premyofibrils of different species and muscle cell types [76, 52, 95]. By utilizing an adapted particle swarm optimization algorithm, we were able to modulate the relative influence of neighboring α-actinin clusters and showed that different interaction dynamics may influence the eventual pattern formed. Although

the current model is only applicable to isolated premyofibrils, an extended phenomenological model can be created which allows our premyofibril α-actinin distribution to align and fuse with neighboring α-actinin while still being constrained to their designated myofibril curve. This alignment and fusion mechanism may have energetic underpinnings where it becomes more energetically favorable in some sense when neighboring z-lines align and lock together. Whether an energetically driven align-lock approach is sufficient to produce the sarcomeric registration found in mature cardiomyocytes has yet to be explored.

In Chapter 3 we successfully simulated a developing myofibril network that dynamically changed over time. The model in its presented form was able to reproduce the variability found in cytoskeletal networks while capturing structural properties that were consistent with previous experimental observations [92, 36]. One such property was the ability to produce cytoskeletal networks in cells of different aspect ratios with maximum traction stresses on the order of 1 kPa [67, 89]. We demonstrated that allowing the force associated with a developing myofibril to vary based on a relative length measure produced more accurate stress values when compared to an absolute length dependence. We were also able to capture qualitatively observed behavior such as the average length of the myofibril bundles within the cytoskeleton increasing with cell aspect ratio in an almost linear manner. At the same time, the number of myofibril bundles created in low aspect ratio cells was found to be larger than the number of bundles in high aspect ratio cells, a quality that can be visually observed but had not been quantitatively described. We believe that one of the components driving the resulting traction stress values is the interplay between the number of myofibrils within the network, the length of the proposed myofibrils, and the relative length dependence as dictated by the cell geometry. Further explorations of this relative length dependence may resolve the discrepancy between our traction stress values and the experimentally observed values for the moderate aspect ratios.

Lastly, Chapter 4 demonstrated how the cytoskeletal model from Chapter 3 could be used

to explore shape changes in the nucleus. Although this is in an early stage of development, the preliminary results demonstrate how modeling the nucleus as an elastically deforming sphere can be combined with our current cytoskeletal model to study the physical interactions between the nucleus and cytoskeleton. This interplay can be captured more accurately in the future by allowing nuclear deformations to change dynamically due to the influence of the changing cytoskeleton. Additionally, there is evidence that genetic mutations may influence the nature of nuclear deformations [25, 123]. Further advancements could include exploring whether alterations in the material properties of the nucleus combined with cytoskeletal interactions are sufficient to produce irregular (non-elliptical) shaped nuclei.

We foresee several additional generalizations that can be made from our modeling approach, two of which will be addressed here. The modeling components proposed have been restricted to individual cells but may be applicable to multiple interacting cells. For instance, while integrins are present in the focal adhesions that anchor myofibril bundles of a single cell, they are also present in intercellular junctions. Within these junctions, integrins serve to anchor individual cells to the extracellular matrix while cadherins anchor cells to one another. These adhesion junctions also contain actin filaments associated with them that provide anchoring and bending in cell sheets. Moreover, sarcomeric registration is present not only in individual cells but also in cell sheets. Given our modeling approach for a single cell, a generalization to interacting cells should be feasible. This would allow us to study self-organization at the tissue scale.

A second application of our model requires us to alter a central modeling assumption. Namely, we considered individual cells that were grown on a flat surface. This allowed us to model the development of myofibril bundles at an approximately planar level, consistent with what has been observed experimentally [11]. However, a flat surface it is not applicable to cells seen in microenvironments. For instance, using a curved surface provides a better experimental setup of cells found in microvessels as opposed to a flat surface. Under

this scenario, myofibril bundles may have an additional degree of freedom and the nucleus becomes a spherical obstruction rather than a circular obstruction. Modeling cells on a curved surface would allow us to explore how this additional degree of freedom influences the cytoskeleton and resulting sarcomeres.

Bibliography

[1] A. Agarwal, J. A. Goss, A. Cho, M. L. McCain, and K. K. Parker. Microfluidic heart on a chip for higher throughput pharmacological studies. *Lab on a Chip*, 13(18):3599–3608, 2013.

[2] S. Ahn, H. A. M. Ardoña, J. U. Lind, F. Eweje, S. L. Kim, G. M. Gonzalez, Q. Liu, J. F. Zimmerman, G. Pyrgiotakis, Z. Zhang, J. Beltran-Huarac, P. Carpinone, B. M. Moudgil, P. Demokritou, and K. K. Parker. Mussel-inspired 3D fiber scaffolds for heart-on-a-chip toxicity studies of engineered nanomaterials. *Analytical and Bioanalytical Chemistry*, 410(24):6141–6154, 2018.

[3] B. Alberts, A. Johnson, J. Lewis, M. Raff, K. Roberts, and P. Walter. *Integrins*. Garland Science, fourth edition, 2002.

[4] P. W. Alford, A. W. Feinberg, S. P. Sheehy, and K. K. Parker. Biohybrid thin films for measuring contractility in engineered cardiovascular muscle. *Biomaterials*, 31(13):3613–3621, 2010.

[5] Y. Asahi, T. Hamada, A. Hattori, K. Matsuura, M. Odaka, F. Nomura, T. Kaneko, Y. Abe, K. Takasuna, A. Sanbuissho, and K. Yasuda. On-chip spatiotemporal electrophysiological analysis of human stem cell derived cardiomyocytes enables quantitative assessment of proarrhythmia in drug development. *Scientific Reports*, 8:14536, 2018.

[6] J. M. G. Aznar, C. Valero, C. Borau, and N. Garijo. Computational mechano-chemobiology: a tool for the design of tissue scaffolds. *Biomanufacturing Reviews*, 1:2, 2016.

[7] B. M. Baker and C. S. Chen. Deconstructing the third dimension - how 3D culture microenvironments alter cellular cues. *Journal of Cell Science*, 125(13):3015, July 2012.

[8] N. Q. Balaban, U. S. Schwarz, D. Riveline, P. Goichberg, G. Tzur, I. Sabanay, D. Mahalu, S. Safran, A. Bershadsky, L. Addadi, and B. Geiger. Force and focal adhesion assembly: a close relationship studied using elastic micropatterned substrates. *Nature Cell Biology*, 3:466–472, 2001.

[9] M. Bathe, C. Heussinger, M. M. A. E. Claessens, A. R. Bausch, and E. Frey. Cytoskeletal Bundle Mechanics. *Biophysical Journal*, 94(8):2955–2964, 2008.

[10] A. D. Bershadsky, N. Q. Balaban, and B. Geiger. Adhesion-Dependent Cell Mechanosensitivity. *Annual Review of Cell and Developmental Biology*, 19(1):677–695, 2003.

[11] S. Y. Boateng and P. H. Goldspink. Assembly and maintenance of the sarcomere night and day. *Cardiovascular Research*, 77(4):667–675, 2008.

[12] M. Böl, S. Reese, K. K. Parker, and E. Kuhl. Computational modeling of muscular thin films for cardiac repair. *Computational Mechanics*, 43(4):535–544, 2009.

[13] C. Bonet, S. K. Maciver, and A. Mozo-Villarías. The regulatory action of α-actinin on actin filaments is enhanced by cofilin. *European Biophysics Journal*, 39(8):1143–1153, July 2010.

[14] C. Borau, R. D. Kamm, and J. M. García-Aznar. A time-dependent phenomenological model for cell mechano-sensing. *Biomechanics and modeling in mechanobiology*, 13(2):451–462, Apr. 2014.

[15] A. L. Bui, T. B. Horwich, and G. C. Fonarow. Epidemiology and risk profile of heart failure. *Nature Reviews Cardiology*, 8:30–41, 2010.

[16] N. Caille, O. Thoumine, Y. Tardy, and J.-J. Meister. Contribution of the nucleus to the mechanical properties of endothelial cells. *Journal of Biomechanics*, 35(2):177–187, 2002.

[17] Q. Chen, G. E. Kirsch, D. Zhang, R. Brugada, J. Brugada, P. Brugada, D. Potenza, A. Moya, M. Borggrefe, G. Breithardt, R. Ortiz-Lopez, Z. Wang, C. Antzelevitch, R. E. O'Brien, E. Schulze-Bahr, M. T. Keating, J. A. Towbin, and Q. Wang. Genetic basis and molecular mechanism for idiopathic ventricular fibrillation. *Nature*, 392(6673):293–296, 1998.

[18] R. J. Chi, S. G. Olenych, K. Kim, and T. C. S. Keller. Smooth muscle α-actinin interaction with smitin. *The International Journal of Biochemistry & Cell Biology*, 37(7):1470–1482, 2005.

[19] K. R. Chien, I. J. Domian, and K. K. Parker. Cardiogenesis and the complex biology of regenerative cardiovascular medicine. *Science*, 322(5907):1494–1497, 2008.

[20] J. Choi, R. Curry, and G. Elkaim. Path Planning Based on Bézier Curve for Autonomous Ground Vehicles. In *Advances in Electrical and Electronics Engineering - IAENG Special Edition of the World Congress on Engineering and Computer Science 2008*, pages 158–166, 2008.

[21] A. Chopra, M. L. Kutys, K. Zhang, W. J. Polacheck, C. C. Sheng, R. J. Luu, J. Eyckmans, J. T. Hinson, J. G. Seidman, C. E. Seidman, and C. S. Chen. Force Generation via beta-Cardiac Myosin, Titin, and alpha-Actinin Drives Cardiac Sarcomere Assembly from Cell-Matrix Adhesions. *Developmental Cell*, 44(1):87–96, 2018.

[22] C. E. Clancy and Y. Rudy. Linking a genetic defect to its cellular phenotype in a cardiac arrhythmia. *Nature*, 400(6744):566–569, 1999.

[23] O. Cohen and S. A. Safran. Theory of frequency response of mechanically driven cardiomyocytes. *Scientific Reports*, 8:2237, 2018.

[24] G. M. Cooper. *Actin, Myosin, and Cell Movement*. Sinauer Associates, second edition, 2000.

[25] J. Q. Core, M. Mehrabi, Z. R. Robinson, A. R. Ochs, L. A. McCarthy, M. V. Zaragoza, and A. Grosberg. Age of heart disease presentation and dysmorphic nuclei in patients with LMNA mutations. *PLOS ONE*, 12(11):e0188256, Nov. 2017.

[26] S. R. Coyer, A. Singh, D. W. Dumbauld, D. A. Calderwood, S. W. Craig, E. Delamarche, and A. J. Garc 'ia. Nanopatterning reveals an ECM area threshold for focal adhesion assembly and force transmission that is regulated by integrin activation and cytoskeleton tension. *Journal of cell science*, 125(Pt 21):5110–5123, Nov. 2012.

[27] J. P. Cranford, T. J. O'Hara, C. T. Villongco, O. M. Hafez, R. C. Blake, J. Loscalzo, J.-L. Fattebert, D. F. Richards, X. Zhang, J. N. Glosli, A. D. McCulloch, D. E. Krummen, F. C. Lightstone, and S. E. Wong. Efficient computational modeling of human ventricular activation and its electrocardiographic representation: A sensitivity study. *Cardiovascular Engineering and Technology*, 9(3):447–467, 2018.

[28] G. A. Dabiri, K. K. Turnacioglu, J. M. Sanger, and J. W. Sanger. Myofibrillogenesis visualized in living embryonic cardiomyocytes. *Proceedings of the National Academy of Sciences*, 94(17):9493–9498, 1997.

[29] J. O. Dada and P. Mendes. Multi-scale modelling and simulation in systems biology. *Integrative Biology*, 3(2):86–96, 2011.

[30] G. Danuser, J. Allard, and A. Mogilner. Mathematical modeling of eukaryotic cell migration: insights beyond experiments. *Annual review of cell and developmental biology*, 29:501–528, 2013.

[31] K. Dasbiswas, S. Majkut, D. E. Discher, and S. A. Safran. Substrate stiffness-modulated registry phase correlations in cardiomyocytes map structural order to coherent beating. *Nature Communications*, 6, 2015.

[32] V. S. Deshpande, R. M. McMeeking, and A. G. Evans. A bio-chemo-mechanical model for cell contractility. *Proceedings of the National Academy of Sciences*, 103(38):14015, Sept. 2006.

[33] J. Deutsch, D. Motlagh, B. Russell, and T. A. Desai. Fabrication of microtextured membranes for cardiac myocyte attachment and orientation. *Journal of Biomedical Materials Research*, 53(3):267–275, 2000.

[34] N. K. Drew, M. A. Eagleson, D. B. B. Jr., K. K. Parker, and A. Grosberg. Metrics for assessing cytoskeletal orientational correlations and consistency. *PLoS computational biology*, 11(4), 2015.

[35] N. K. Drew and A. Grosberg. *Methods of Myofibrillogenesis Modeling*, pages 75–91. Springer New York, New York, NY, 2015.

[36] N. K. Drew, N. E. Johnsen, J. Q. Core, and A. Grosberg. Multiscale characterization of engineered cardiac tissue architecture. *Journal of Biomechanical Engineering*, 138(11):111003, 2016.

[37] J. S. Duncan, F. A. Lee, A. W. M. Smeulders, and B. L. Zaret. A bending energy model for measurement of cardiac shape deformity. *IEEE Transactions on Medical Imaging*, 10(3):307–320, 1991.

[38] K. Duval, H. Grover, L.-H. Han, Y. Mou, A. F. Pegoraro, J. Fredberg, and Z. Chen. Modeling Physiological Events in 2D vs. 3D Cell Culture. *Physiology (Bethesda, Md.)*, 32(4):266–277, July 2017.

[39] R. C. Eberhart, Y. Shi, and J. Kennedy. *Swarm Intelligence*. Morgan Kaufmann, Burlington, MA, 2001.

[40] L. Edelstein-Keshet. A mathematical approach to cytoskeletal assembly. *European Biophysics Journal*, 27:521–531, 1998.

[41] E. Ehler. Cardiac cytoarchitecture - why the "hardware" is important for heart function! *Biochimica et biophysica acta*, 1863(7 Pt B):1857–1863, July 2016.

[42] A. Engelbrecht. Particle swarm optimization: Velocity initialization. In *2012 IEEE Congress on Evolutionary Computation*, pages 1–8, 2012.

[43] X. Fan, B. G. Hughes, M. A. M. Ali, W. J. Cho, W. Lopez, and R. Schulz. Dynamic Alterations to alpha-Actinin Accompanying Sarcomere Disassembly and Reassembly during Cardiomyocyte Mitosis. *PLOS ONE*, 10(6), 2015.

[44] A. W. Feinberg, A. Feigel, S. S. Shevkoplyas, S. Sheehy, G. M. Whitesides, and K. K. Parker. Muscular thin films for building actuators and powering devices. *Science*, 317(5843):1366–1370, 2007.

[45] T. S. Fraley, C. B. Pereira, T. C. Tran, C. Singleton, and J. A. Greenwood. Phosphoinositide binding regulates α-actinin dynamics: Mechanism for modulating cytoskeletal remodeling. *Journal of Biological Chemistry*, 280:15479–15482, 2005.

[46] B. M. Friedrich, A. Buxboim, D. E. Discher, and S. A. Safran. Striated acto-myosin fibers can reorganize and register in response to elastic interactions with the matrix. *Biophysical journal*, 100(11):2706–2715, June 2011.

[47] B. M. Friedrich, E. Fischer-Friedrich, N. S. Gov, and S. A. Safran. Sarcomeric Pattern Formation by Actin Cluster Coalescence. *PLOS Computational Biology*, 8(6), 2012.

[48] A. Fruleux and R. J. Hawkins. Physical role for the nucleus in cell migration. *Journal of Physics: Condensed Matter*, 28(36), 2016.

[49] A. M. Gerdes. Cardiac myocyte remodeling in hypertrophy and progression to failure. *Journal of Cardiac Failure*, 8(6):S264–S268, 2002.

[50] A. M. Gerdes, S. E. Kellerman, J. A. Moore, K. E. Muffly, L. C. Clark, P. Y. Reaves, K. B. Malec, P. P. McKeown, and D. D. Schocken. Structural remodeling of cardiac myocytes in patients with ischemic cardiomyopathy. *Circulation*, 86(2):426–430, 1992.

[51] M. Golob, R. L. Moss, and N. C. Chesler. Cardiac tissue structure, properties, and performance: A materials science perspective. *Annals of Biomedical Engineering*, 42(10):2003–2013, 2014.

[52] M. Golson, J. M. Sanger, and J. W. Sanger. Inhibitors arrest myofibrillogenesis in skeletal muscle cells at early stages of assembly. *Cell motility and the cytoskeleton*, 59:1–16, Sept. 2004.

[53] R. A. Greenbaum, S. Y. Ho, D. G. Gibson, A. E. Becker, and R. H. Anderson. Left ventricular fibre architecture in man. *British heart journal*, 45(3):248–263, 1981.

[54] A. Grosberg, P. W. Alford, M. L. McCain, and K. K. Parker. Ensembles of engineered cardiac tissues for physiological and pharmacological study: Heart on a chip. *Lab on a Chip*, 11(24):4165–4173, 2011.

[55] A. Grosberg, P.-L. Kuo, C.-L. Guo, N. A. Geisse, M.-A. Bray, W. J. Adams, S. P. Sheehy, and K. K. Parker. Self-organization of muscle cell structure and function. *PLOS Computational Biology*, 7(2):1–15, 2011.

[56] H. Hamada, F. Nomura, T. Kaneko, K. Yasuda, and M. Okamoto. Exploring the implicit interlayer regulatory mechanism between cells and tissue: Stochastic mathematical analyses of the spontaneous ordering in beating synchronization. *Biosystems*, 111(3):208–215, 2013.

[57] T. Hayashi, T. Tokihiro, H. Kurihara, and K. Yasuda. Community effect of cardiomyocytes in beating rhythms is determined by stable cells. *Scientific Reports*, 7:15450, 2017.

[58] N. Hersch, B. Wolters, G. Dreissen, R. Springer, N. Kirchgeßner, R. Merkel, and B. Hoffmann. The constant beat: cardiomyocytes adapt their forces by equal contraction upon environmental stiffening. *Biology Open*, 2(3):351–361, 2013.

[59] Y. Hu, V. Gurev, J. Constantino, J. D. Bayer, and N. A. Trayanova. Effects of mechano-electric feedback on scroll wave stability in human ventricular fibrillation. *PloS one*, 8(4), 2013.

[60] A. D. Kaiser, D. M. McQueen, and C. S. Peskin. Modeling the Mitral Valve. *arXiv e-prints*, page arXiv:1902.00018, 2019.

[61] T. Kaneko, K. Kojima, and K. Yasuda. An on-chip cardiomyocyte cell network assay for stable drug screening regarding community effect of cell network size. *Analyst*, 132:892–898, 2007.

[62] E. Kassianidou, C. A. Brand, U. S. Schwarz, and S. Kumar. Geometry and network connectivity govern the mechanics of stress fibers. *Proceedings of the National Academy of Sciences*, page 201606649, Feb. 2017.

[63] D.-H. Kim, E. A. Lipke, P. Kim, R. Cheong, S. Thompson, M. Delannoy, K.-Y. Suh, L. Tung, and A. Levchenko. Nanoscale cues regulate the structure and function of macroscopic cardiac tissue constructs. *Proceedings of the National Academy of Sciences*, 107(2):565–570, 2010.

[64] M. B. Knight, N. K. Drew, L. A. McCarthy, and A. Grosberg. Emergent Global Contractile Force in Cardiac Tissues. *Biophysical journal*, 110(7):1615–1624, Apr. 2016.

[65] R. Knöll, M. Hoshijima, and K. R. Chien. Z-line proteins: implications for additional functions. *European Heart Journal Supplements*, 4(Supplement I):I13–I17, Dec. 2002.

[66] K. Kojima, T. Kaneko, and K. Yasuda. Stability of beating frequency in cardiac myocytes by their community effect measured by agarose microchamber chip. *Journal of Nanobiotechnology*, 3(1):4, 2005.

[67] P.-L. Kuo, H. Lee, M.-A. Bray, N. A. Geisse, Y.-T. Huang, W. J. Adams, S. P. Sheehy, and K. K. Parker. Myocyte shape regulates lateral registry of sarcomeres and contractility. *The American Journal of Pathology*, 181(6):2030–2037, 2012.

[68] J. Lammerding. Mechanics of the nucleus. *Comprehensive Physiology*, 1(2):783–807, 2011.

[69] J. Liang, B. Huang, G. Yuan, Y. Chen, F. Liang, H. Zeng, S. Zheng, L. Cao, D. Geng, and S. Zhou. Stretch-activated channel Piezo1 is up-regulated in failure heart and cardiomyocyte stimulated by AngII. *American journal of translational research*, 9(6):2945–2955, June 2017.

[70] O. Lieleg, M. M. A. E. Claessens, and A. R. Bausch. Structure and dynamics of cross-linked actin networks. *Soft Matter*, 6:218–225, 2010.

[71] J. S. Lowe and P. G. Anderson. *Stevens & Lowe's Human Histology*, chapter Chapter 5 - Contractile Cells, pages 71–83. Mosby, Philadelphia, fourth edition edition, 2015.

[72] L. Lu, S. J. Oswald, H. Ngu, and F. C.-P. Yin. Mechanical properties of actin stress fibers in living cells. *Biophysical Journal*, 2008.

[73] S. Lu and R. Horowits. Role of nonmuscle myosin IIB and N-RAP in cell spreading and myofibril assembly in primary mouse cardiomyocytes. *Cell motility and the cytoskeleton*, 65(9):747–761, Sept. 2008.

[74] S. Majkut, T. Idema, J. Swift, C. Krieger, A. Liu, and D. E. Discher. Heart-Specific Stiffening in Early Embryos Parallels Matrix and Myosin Expression to Optimize Beating. *Current Biology*, 23(23):2434–2439, 2013.

[75] D. Manas and S. Brett. Organ Donation and Transplantation Activity Report 2014/15, 2014.

[76] S. M. Manisastry, K. J. M. Zaal, and R. Horowits. Myofibril assembly visualized by imaging N-RAP, alpha-actinin, and actin in living cardiomyocytes. *Experimental cell research*, 315(12):2126–2139, July 2009.

[77] H. Mansour, P. P. de Tombe, A. M. Samarel, and B. Russell. Restoration of resting sarcomere length after uniaxial static strain is regulated by protein kinase Cϵ and focal adhesion kinase. *Circulation Research*, 94:642–649, 2004.

[78] F. Marini and B. Walczak. Particle swarm optimization (PSO). A tutorial. *Chemometrics and Intelligent Laboratory Systems*, 149:153–165, 2015.

[79] J. Mayourian, E. A. Sobie, and K. D. Costa. An Introduction to Computational Modeling of Cardiac Electrophysiology and Arrhythmogenicity. *Methods in molecular biology (Clifton, N.J.)*, 1816:17–35, 2018.

[80] M. L. McCain, H. Yuan, F. S. Pasqualini, P. H. Campbell, and K. K. Parker. Matrix elasticity regulates the optimal cardiac myocyte shape for contractility. *American journal of physiology. Heart and circulatory physiology*, 306(11):H1525–H1539, June 2014.

[81] M. Mills, N. Yang, R. Weinberger, D. L. V. Woude, A. H. Beggs, S. Easteal, and K. North. Differential expression of the actin-binding proteins, α-actinin-2 and -3, in different species: implications for the evolution of functional redundancy. *Human Molecular Genetics*, 10(13):1335–1346, June 2001.

[82] P. Moreo, J. M. García-Aznar, and M. Doblaré. Modeling mechanosensing and its effect on the migration and proliferation of adherent cells. *Acta Biomaterialia*, 4(3):613–621, 2008.

[83] T. A. Morris, J. Naik, K. S. Fibben, X. Kong, T. Kiyono, K. Yokomori, and A. Grosberg. Striated myocyte structural integrity: Automated analysis of sarcomeric z-discs. *PLOS Computational Biology*, 16(3):e1007676, Mar. 2020.

[84] M. Necula and J. Kuret. Pseudophosphorylation and glycation of tau protein enhance but do not trigger fibrillization in vitro. *The Journal of Biological Chemistry*, 279:49694–49703, 2004.

[85] D. Nickerson, N. Smith, and P. Hunter. New developments in a strongly coupled cardiac electromechanical model. *EP Europace*, 7(s2):S118–S127, 2005.

[86] A. Nicolas, A. Besser, and S. A. Safran. Dynamics of cellular focal adhesions on deformable substrates: Consequences for cell force microscopy. *Biophysical Journal*, 95(2):527–539, 2008.

[87] D. Noble and P.-J. Noble. Reconstruction of cellular mechanisms of genetically-based arrhythmias. *Journal of Physiology*, 518(2-3P), 1999.

[88] I. L. Novak, B. M. Slepchenko, A. Mogilner, and L. M. Loew. Cooperativity between cell contractility and adhesion. *Physical Review Letters*, 93:268109, 2004.

[89] P. W. Oakes, S. Banerjee, M. C. Marchetti, and M. L. Gardel. Geometry regulates traction stresses in adherent cells. *Biophysical Journal*, 107(4):825–833, 2014.

[90] Z. Orfanos, K. Leonard, C. Elliott, A. Katzemich, B. Bullard, and J. Sparrow. Sallimus and the Dynamics of Sarcomere Assembly in Drosophila Flight Muscles. *Journal of Molecular Biology*, 427(12):2151–2158, 2015.

[91] M. Ottolia, N. Torres, J. H. B. Bridge, K. D. Philipson, and J. I. Goldhaber. Na/Ca exchange and contraction of the heart. *Journal of molecular and cellular cardiology*, 61:28–33, Aug. 2013.

[92] K. K. Parker, J. Tan, C. S. Chen, and L. Tung. Myofibrillar Architecture in Engineered Cardiac Myocytes. *Circulation Research*, 103(4):340–342, June 2008.

[93] C. L. Perreault, O. H. Bing, W. W. Brooks, B. J. Ransil, and J. P. Morgan. Differential effects of cardiac hypertrophy and failure on right versus left ventricular calcium activation. *Circulation Research*, 67(3):707–712, 1990.

[94] T. Pong, W. J. Adams, M.-A. Bray, A. W. Feinberg, S. P. Sheehy, A. A. Werdich, and K. K. Parker. Hierarchical architecture influences calcium dynamics in engineered cardiac muscle. *Experimental Biology and Medicine*, 236(3):366–373, 2011.

[95] M. C. Reedy and C. Beall. Ultrastructure of Developing Flight Muscle in Drosophila. I. Assembly of Myofibrils. *Developmental Biology*, 160(2):443–465, 1993.

[96] D. Rhee, J. M. Sanger, and J. W. Sanger. The premyofibril: Evidence for its role in myofibrillogenesis. *Cell motility and the cytoskeleton*, 28(1):1–24, 1994.

[97] A. J. S. Ribeiro, Y.-S. Ang, J.-D. Fu, R. N. Rivas, T. M. A. Mohamed, G. C. Higgs, D. Srivastava, and B. L. Pruitt. Contractility of single cardiomyocytes differentiated from pluripotent stem cells depends on physiological shape and substrate stiffness. *Proceedings of the National Academy of Sciences*, 112(41):12705–12710, 2015.

[98] H. Ritchie and M. Roser. Causes of Death. *Our World in Data*, 2019. https://ourworldindata.org/causes-of-death.

[99] D. Rohmer, A. Sitek, and G. Gullberg. Reconstruction and visualization of fiber and sheet structure with regularized tensor diffusion MRI in the human heart. *Investigative Radiology*, 42:777–784, 2007.

[100] B. Russell, D. Motlagh, and W. W. Ashley. Form follows function: how muscle shape is regulated by work. *Journal of Applied Physiology*, 88(3):1127–1132, 2000.

[101] S. Safaei, C. P. Bradley, V. Suresh, K. Mithraratne, A. Muller, H. Ho, D. Ladd, L. R. Hellevik, S. W. Omholt, J. G. Chase, L. O. M "uller, S. M. Watanabe, P. J. Blanco, B. de Bono, and P. J. Hunter. Roadmap for cardiovascular circulation model. *The Journal of physiology*, 594(23):6909–6928, Dec. 2016.

[102] J. M. Sanger, B. Mittal, M. B. Pochapin, and J. W. Sanger. Myofibrillogenesis in living cells microinjected with fluorescently labeled alpha-actinin. *The Journal of cell biology*, 102(6):2053–2066, June 1986.

[103] J. W. Sanger, S. Kang, C. C. Siebrands, N. Freeman, A. Du, J. Wang, A. L. Stout, and J. M. Sanger. How to build a myofibril. *Journal of Muscle Research & Cell Motility*, 26(6):343, 2006.

[104] J. W. Sanger, J. Wang, B. Holloway, A. Du, and J. M. Sanger. Myofibrillogenesis in skeletal muscle cells in zebrafish. *Cell motility and the cytoskeleton*, 66(8):556–566, Aug. 2009.

[105] P. Savadjiev, G. J. Strijkers, A. J. Bakermans, E. Piuze, S. W. Zucker, and K. Siddiqi. Heart wall myofibers are arranged in minimal surfaces to optimize organ function. *Proceedings of the National Academy of Sciences of the United States of America*, 109(24):9248–9253, June 2012.

[106] U. S. Schwarz and T. E. I. B. Bischofs. Focal adhesions as mechanosensors: The two-spring model. *Biosystems*, 83(2-3):225–232, 2006.

[107] V. Sequeira, L. L. A. M. Nijenkamp, J. A. Regan, and J. van der Velden. The physiological role of cardiac cytoskeleton and its alterations in heart failure. *Biochimica et Biophysica Acta (BBA) - Biomembranes*, 1838(2):700–722, 2014.

[108] S. P. Sheehy, A. Grosberg, and K. K. Parker. The contribution of cellular mechanotransduction to cardiomyocyte form and function. *Biomechanics and modeling in mechanobiology*, 11(8):1227–1239, Nov. 2012.

[109] W. F. Sherman and A. Grosberg. Exploring cardiac form and function: A length-scale computational biology approach. *WIREs Systems Biology and Medicine*, 12(2):e1470, 2020.

[110] J. Shim, A. Grosberg, J. C. Nawroth, K. K. Parker, and K. Bertoldi. Modeling of cardiac muscle thin films: Pre-stretch, passive and active behavior. *Journal of Biomechanics*, 45(5):832–841, 2012.

[111] R. Shimkunas, Z. Zhang, J. F. Wenk, M. Soleimani, M. Khazalpour, G. Acevedo-Bolton, G. Wang, D. Saloner, R. Mishra, A. W. Wallace, L. Ge, A. J. Baker, J. M. Guccione, and M. B. Ratcliffe. Left ventricular myocardial contractility is depressed in the borderzone after posterolateral myocardial infarction. *The Annals of Thoracic Surgery*, 95(5):1619–1625, 2013.

[112] J. R. Silva. How to Connect Cardiac Excitation to the Atomic Interactions of Ion Channels. *Biophysical journal*, 114(2):259–266, Jan. 2018.

[113] R. Singhvi, G. Stephanopoulos, and D. I. C. Wang. Effects of substratum morphology on cell physiology. *Biotechnology and Bioengineering*, 43(8):764–771, 1994.

[114] B. Sjöblom, A. Salmazo, and K. Djinović-Carugo. α-Actinin structure and regulation. *Cellular and Molecular Life Sciences*, 65(17):2688, Sept. 2008.

[115] V. G. Soukhovolsky, Y. D. Ivanova, K. Shulman, V. F. Mazharov, I. V. Tarasova, O. V. Tarasova, and R. G. Khlebopros. The population dynamics of cancer incidence: The model of a second-order phase transition. *Biophysics*, 60(4):639–646, 2015.

[116] J. Stehlik, L. B. Edwards, A. Y. Kucheryavaya, C. Benden, J. D. Christie, F. Dobbels, R. Kirk, A. O. Rahmel, and M. I. Hertz. The registry of the international society for heart and lung transplantation: Twenty-eighth adult heart transplant report–2011. *The Journal of Heart and Lung Transplantation*, 30(10):1078–1094, 2011.

[117] D. Streeter. Gross morphology and fiber geometry of the heart. 1979.

[118] D. D. Streeter, H. M. Spotnitz, D. P. Patel, J. Ross, and E. H. Sonnenblick. Fiber Orientation in the Canine Left Ventricle during Diastole and Systole. *Circulation Research*, 24(3):339–347, 1969.

[119] J. Sun, J. Tang, and J. Ding. Cell orientation on a stripe-micropatterned surface. *Chinese Science Bulletin*, 54(18):3154–3159, 2009.

[120] J. L. Tan, J. Tien, D. M. Pirone, D. S. Gray, K. Bhadriraju, and C. S. Chen. Cells lying on a bed of microneedles: An approach to isolate mechanical force. *PNAS*, 100(4):1484–1489, 2003.

[121] Y. Tatara. On Compression of Rubber Elastic Sphere Over a Large Range of Displacements - Part 1: Theoretical Study. *Journal of Engineering Materials and Technology*, 113(3):285–291, 1991.

[122] N. Thavandiran, S. S. Nunes, Y. Xiao, and M. Radisic. Topological and electrical control of cardiac differentiation and assembly. *Stem Cell Research & Therapy*, 4(1):14, 2013.

[123] R. D. H. Tran, M. Siemens, C. H. H. Nguyen, A. R. Ochs, M. V. Zaragoza, and A. Grosberg. The Effect of Cyclic Strain on Human Fibroblasts With Lamin A/C Mutations and Its Relation to Heart Disease. *Journal of Biomechanical Engineering*, 142(6):061002, Jan. 2020.

[124] N. A. Trayanova and R. Winslow. Whole-heart modeling: Applications to cardiac electrophysiology and electromechanics. *Circulation Research*, 108(1):113–128, 2011.

[125] A. Umeno and S. Ueno. Quantitative analysis of adherent cell orientation influenced by strong magnetic fields. *IEEE Transactions on NanoBioscience*, 2(1):26–28, 2003.

[126] T. P. Usyk and A. D. McCulloch. Relationship between regional shortening and asynchronous electrical activation in a three-dimensional model of ventricular electromechanics. *Journal of Cardiovascular Electrophysiology*, 14(s10):S196–S202, 2003.

[127] H. M. W. van der Velden and H. J. Jongsma. Cardiac gap junctions and connexins: their role in atrial fibrillation and potential as therapeutic targets. *Cardiovascular Research*, 54(2):270–279, 2002.

[128] R. C. Veltkamp and W. Wesselink. Modeling 3D Curves of Minimal Energy. *Computer Graphics Forum*, 14(3):97–110, 1995.

[129] M. Versaevel, T. Grevesse, and S. Gabriele. Spatial coordination between cell and nuclear shape within micropatterned endothelial cells. *Nature Communications*, 3:671, 2012.

[130] C. T. Villongco, D. E. Krummen, J. H. Omens, and A. D. McCulloch. Non-invasive, model-based measures of ventricular electrical dyssynchrony for predicting CRT outcomes. *EP Europace*, 18(suppl_4):iv104–iv112, 2016.

[131] R. Vishavkarma, S. Raghavan, C. Kuyyamudi, A. Majumder, J. Dhawan, and P. A. Pullarkat. Role of actin filaments in correlating nuclear shape and cell spreading. *PLOS ONE*, 9(9):1–13, 2014.

[132] G. Vunjak-Novakovic, N. Tandon, A. Godier, R. Maidhof, A. Marsano, T. P. Martens, and M. Radisic. Challenges in cardiac tissue engineering. *Tissue Engineering Part B: Reviews*, 16(2):169–187, 2009.

[133] J. Wang, N. Shaner, B. Mittal, Q. Zhou, J. Chen, J. M. Sanger, and J. W. Sanger. Dynamics of Z-band based proteins in developing skeletal muscle cells. *Cell motility and the cytoskeleton*, 61(1):34–48, 2005.

[134] T. Washio, K. Yoneda, J. ichi Okada, T. Kariya, S. Sugiura, and T. Hisada. Ventricular fiber optimization utilizing the branching structure. *International Journal for Numerical Methods in Biomedical Engineering*, 32(7), 2016.

[135] H. Watanabe, S. Sugiura, H. Kafuku, and T. Hisada. Multiphysics simulation of left ventricular filling dynamics using fluid-structure interaction finite element method. *Biophysical journal*, 87(3):2074–2085, 2004.

[136] M. Weitkunat, M. Brasse, A. R. Bausch, and F. Schnorrer. Mechanical tension and spontaneous muscle twitching precede the formation of cross-striated muscle in vivo. *Development (Cambridge, England)*, 144(7):1261–1272, Apr. 2017.

[137] J. White, M. V. Barro, H. P. Makarenkova, J. W. Sanger, and J. M. Sanger. Localization of sarcomeric proteins during myofibril assembly in cultured mouse primary skeletal myotubes. *Anatomical record (Hoboken, N.J. : 2007)*, 297(9):1571–1584, Sept. 2014.

[138] R. Wilders, H. J. Jongsma, and A. C. van Ginneken. Pacemaker activity of the rabbit sinoatrial node. A comparison of mathematical models. *Biophysical Journal*, 60(5):1202–1216, 1991.

[139] J. Xin, G. Chen, and Y. Hai. A Particle Swarm Optimizer with Multi-stage Linearly-Decreasing Inertia Weight. In *2009 International Joint Conference on Computational Sciences and Optimization*, volume 1, pages 505–508, 2009.

[140] K. C. Yan, K. Nair, and W. Sun. Three dimensional multi-scale modelling and analysis of cell damage in cell-encapsulated alginate constructs. *Journal of Biomechanics*, 43(6):1031–1038, 2010.

[141] V. Yarov-Yarovoy, T. W. Allen, and C. E. Clancy. Computational models for predictive cardiac ion channel pharmacology. *Drug Discovery Today: Disease Models*, 14:3–10, 2014.

[142] J.-G. Yu and B. Russell. Cardiomyocyte Remodeling and Sarcomere Addition after Uniaxial Static Strain In Vitro. *Journal of Histochemistry & Cytochemistry*, 53(7):839–844, 2005.

[143] J. K. Yu, W. Franceschi, Q. Huang, F. Pashakhanloo, P. M. Boyle, and N. A. Trayanova. A comprehensive, multiscale framework for evaluation of arrhythmias arising from cell therapy in the whole post-myocardial infarcted heart. *Scientific Reports*, 9:9238, 2019.

[144] H. Yuan, B. Marzban, and K. K. Parker. Myofibrils in Cardiomyocytes Tend to Assemble Along the Maximal Principle Stress Directions. *Journal of biomechanical engineering*, 139(12):1210101–1210108, Dec. 2017.

[145] I. Zadorozhnyi, H. Hlukhova, Y. Kutovyi, V. Handziuk, N. Naumova, A. Offenhaeusser, and S. Vitusevich. Towards pharmacological treatment screening of cardiomyocyte cells using Si nanowire FETs. *Biosensors and Bioelectronics*, 137:229–235, 2019.

[146] B. Zhang, Y. Xiao, A. Hsieh, N. Thavandiran, and M. Radisic. Micro- and nanotechnology in cardiovascular tissue engineering. *Nanotechnology*, 22(49):494003, 2011.